

TABLE OF CONTENTS

	<u>Page</u>	
SUMMARY	1	1/A7
INTRODUCTION	1	1/A7
SYMBOLS	4	1/A10
METHOD OF ANALYSIS	8	1/A14
Problem Description	8	1/A14
The Flowfield Equations	13	1/B5
Turbulence Closure Modeling	20	1/B12
FINITE ELEMENT SOLUTION ALGORITHM	26	1/C4
COMOC COMPUTER PROGRAM	30	1/C8
NUMERICAL RESULTS	32	1/C10
Symmetry Plane Analysis of A Slot Nozzle - Jet Flap Flow	32	1/C10
Acoustically Modified Planar Jet Flap	39	1/D3
Recirculating Flow Within A Porous Slot	45	1/D9
An Elementary Three-Dimensional Evaluation	46	1/D10
CONCLUDING REMARKS	51	1/E1
APPENDIX	52	1/E2
REFERENCES ...	62	1/E12

ILLUSTRATIONS

<u>Figure</u>	<u>Page</u>
1. Schematic of Representative Jet Flow Patterns Over Wing/Flap Surface, $M_\infty = 0.8$ (Ref. 18).....	8 1/A14
2. Three-Dimensional Representation of Rectangular Slot Injector-Planar Jet Flap Configuration	15 1/B7
3. Two-Dimensional Symmetry Plane Flowfield For Rectangular Slot Nozzle-Planar Jet Flap Configuration	17 1/B9
4. Porous Slot Flow Solution Domain	19 1/B11
5. COMOC Macro Structure	31 1/C9
6. Two-Dimensional Flowfield Specifications For Rectangular Slot Nozzle-Planar Jet Flap Configuration	33 1/C11
7. Development of Turbulent Boundary Layer Over Jet Flap	35 1/C13
8. Longitudinal Velocity Profiles Downstream of Jet Flap	36 1/C14
9. Turbulent Velocity Profiles Downstream of Jet Flap	37 1/D1
10. Mean Flow Velocity Profiles Downstream of Jet Flap Trailing Edge	38 1/D2
11. Turbulent Kinetic Energy Profiles Downstream of Jet Flap Trailing Edge	40 1/D4
12. Influence of Porous Surface Treatment on Turbulent Flow	41 1/D5
13. Finite Element Discretization And Boundary Conditions For Slot Region Recirculating Flow Analysis	45 1/D9
14. Computed Steady Flow Streamline Distributions For Turbulent Flow Over A Jet-Flap Slot	47 1/D11
15. Finite Element Discretization For Three-Dimensional Solution	49 1/D13
16. Computed \bar{u}_1 Distribution at Flap Trailing Edge	49 1/D13
17. Computed Turbulence Kinetic Energy Distributions	50 1/D14

<u>Figure</u>	<u>Page</u>	
A.1 Finite Element Solution Convergence	54	1/E4
A.2 Finite Element Boundary Layer Discretizations	55	1/E5
A.3 Transition Location Influence On Skin Friction, Wieghardt Flat Plate Flow, MLT	56	1/E6
A.4 Longitudinal Velocity Profiles, Wieghardt Flat Plate Flow, MLT	58	1/E8
A.5 Longitudinal Velocity Profiles, Bradshaw Relaxing Flow, MLT	59	1/E9
A.6 Longitudinal Velocity Profiles, Bradshaw Relaxing Flow, TKE	60	1/E10
A.7 Boundary Layer Parameters, Bradshaw Relaxing Flow	61	1/E11

TABLES

<u>Table</u>	<u>Page</u>	
1. Coefficients In TKE Closure Model	24	1/C2
2. Porosity - Induced Jet Flap Flowfield Modifications.....	43	1/D7
3. Distributions Of Mean Flow And Turbulence Velocities Within Initial Secondary Mixing Region As Function Of Simulated Flap Surface Porosity	44	1/D8

Item 230-14-14

NAS 1.26: 2931

DEC 13 1977

NASA Contractor Report 2931

COMPLETED

ORIGINAL

Finite Element Analysis of Aeroacoustic Jet-Flap Flows

A. J. Baker and P. D. Manhardt

CONTRACT NAS1-14282
DECEMBER 1977

NASA

71

NASA Contractor Report 2931

Finite Element Analysis of Aeroacoustic Jet-Flap Flows

A. J. Baker and P. D. Manhardt
Computational Mechanics Consultants, Inc.
Knoxville, Tennessee

Prepared for
Langley Research Center
under Contract NAS1-14282



National Aeronautics
and Space Administration

Scientific and Technical
Information Office

1977

BLANK PAGE

BLANK PAGE

FINITE ELEMENT ANALYSIS OF AEROACOUSTIC JET-FLAP FLOWS

By

A.J. Baker and P.D. Manhardt

Computational Mechanics Consultants

Knoxville, TN

SUMMARY

A computational analysis has been performed on the steady, turbulent aerodynamic flowfields associated with a basic jet-blown flap configuration. For regions devoid of flow separation, a parabolic approximation to the governing time-averaged Navier-Stokes equations is applied, which renders solution amenable to a downstream marching technique. Numerical results are presented for the flow on the symmetry plane of a rectangular slot-nozzle planar jet flap geometry, including detailed prediction of flowfield evolution within the secondary mixing region immediately downstream of the flap trailing edge. Using a two equation turbulence kinetic energy closure model, the numerical results predict rapid generation and decay of large spatial gradients in mean and correlated fluctuating velocity components within the immediate wake region. Modifications to the trailing edge turbulent flow structure, as induced by a simulated porous surface treatment of the flap, are evaluated using a hybrid turbulence closure model. A numerical analysis of the recirculating flow within a representative discrete slot in the surface is evaluated using a complete two-dimensional, time-averaged Navier-Stokes equation set. The parabolic analysis for a smooth flap is extended in an introductory manner to a finite span three-dimensional jet-flap flow. The results of the study are presented in this report.

INTRODUCTION

The use of directed jet flows is common in the design of aerodynamic lift systems. Examples include the leading edge slat-trailing edge flap configurations characteristic of current transport technology, as well as the lower and/or upper-surface blown flap geometries considered for STOL aircraft. In each instance, high momentum flow is directed generally tangential to an aerodynamic surface. Such lift augmentation systems result in noise sources being generated by flow interaction with the lifting surface and equilibration with the free stream. With the progress made in noise reduction of propulsion system components, the noise floor associated with the next generation of propulsive lift systems may well be constrained by the aeroacoustics of the fundamental jet-flap flowfield.

Experimental testing of elementary configurations has been employed to characterize the aeroacoustic sources associated with the basic jet-flap flow in an upper surface blowing (USB) orientation. Gruschka and Schrecker (ref. 1) evaluated a USB geometry comprised of a rectangular jet issuing over a planar flap with sharp trailing edge, and compared measured noise intensities with free jet results. Their data bear out the U^6 law for free jets, first noted by Lighthill (ref. 2,3), and determined a 6th power law for the flap cases. The secondary flow mixing region, immediately downstream of the flap trailing edge contained a dominant noise source. Reshotko et al., (ref. 4) tested a small USB model having a deflected circular jet issuing over a wing section, to determine the acoustic efficiency of the wing as a noise shield. The results showed increased effectiveness with increasing frequency similar to the results of Hayden (ref. 5). An extensive investigation of aerodynamic and acoustic phenomena of a slot nozzle and variable length straight flap was performed by Patterson et al. (ref. 6). They measured free field acoustic response, reverberation chamber acoustics, and utilized hot film anemometry and flow visualization techniques to correlate noise with flow perturbation phenomena. For the geometry tested, a maximum sound power level (SPL) occurred for a flap length of approximately 10 slot heights. An instability condition appeared for this case, as verified by flow visualization and hot film data. Longer flap lengths were determined to produce noise levels closer to the free jet measurements. Becker and Maus (ref. 7) report results of a comprehensive experimental project on the rectangular slot nozzle-planar flap geometry similar to reference 1. Using near and farfield microphone locations and a cross-correlation technique, they determined two extrema in acoustic source strength within the secondary mixing region, one located directly adjacent to the flap trailing edge. Detailed mean and fluctuating velocity correlation measurements indicate the turbulence structure in both mixing regions is highly anisotropic, and that sharp peaks in turbulence quantities occurred immediately downstream of the trailing edge. These rapidly dispersed as the flow proceeded into the wake.

These results generally indicate that a large portion of the fly-over noise associated with a USB equipped aircraft will be generated within the primary and secondary mixing regions. For the latter, the turbulent mixing flow and resultant acoustic source distribution is strongly dependent upon the boundary layer flow immediately preceeding the trailing edge (cf., ref. 8). Hayden, et al., (ref. 5, 9) evaluated a variable impedance flap surface to reduce the noise intensity associated with a USB configuration. Penalties encountered in aerodynamic performance of the early systems were significantly reduced in more recent configurations, employing a cavity-backed porous mesh surface (ref. 10), while retaining the favorable broadband farfield noise reduction of 3 to 10 dB over a wide frequency range and for large turning angle. Many additional studies on powered and unpowered configuration noise measurements, as a function of flow parameters are reported (ref. 11-18) including standard configurations, and various aerodynamic components such as blown flaps, cavities, d-type surfaces, trailing edge interaction, and three-dimensional effects.

The results of these studies confirm the dominance of the jet flap flows as noise sources. A theoretical analysis would be directed at characterization of the basic mechanisms, and would require detailed information regarding the associated turbulent flowfield structure, particularly in the wake region downstream of the flap trailing edge. Assuming the appropriateness of time-averaging, such data is potentially determinable by numerical solution of appropriate subsystems of the governing Navier-Stokes equations. For attached aerodynamic flows, the appropriate system is the boundary layer equation set, the numerical solution to which is routinely accomplished using mixing length theory for turbulence closure and any of several available solution algorithms. For free-mixing shear layer flows, as occur in the primary and downstream secondary mixing regions, the boundary layer set coupled with a turbulence kinetic energy closure model and algebraic length scale, is appropriate for a symmetric geometry. The wake flow within the immediate vicinity of the trailing edge is significantly more complex, and a complete analysis in the general case would require use of the full Navier-Stokes equation set. Such analysis could be extremely expensive, however, and simplifications have been proposed. For example, Melnik and Chow (ref. 19) employ a matched asymptotic analysis to characterize the trailing edge flowfield in a triple deck structure for laminar flows, with extension to turbulent flows for a symmetric geometry (ref. 19, 20). Various forms of the boundary layer equation set have been employed as well for symmetric geometries (c.f., ref. 21). Numerical predictions for turbulent flows have been started somewhat downstream of the trailing edge, where the velocity minimum moderated (c.f., ref. 22).

The present approach is to establish a parabolic approximation to the Navier-Stokes equation set by employing an order of magnitude analysis. The boundary layer equations are a simplified subset of the developed parabolic system, the use of which is not constrained to a symmetric geometry. A two-equation turbulence kinetic energy-dissipation function model is employed to close the developed system for turbulence phenomena. For aeroacoustic flows over flaps with sharp trailing edges, hence devoid of flowfield separation, the developed equation system can be marched directly off the flap surface into the trailing edge wake. Non-equilibrium turbulence phenomena within the immediate wake flow is allowed, such that local extrema in the turbulence phenomena can be predicted. The influence of a porous-acoustic treatment of the flap surface is simulated by appropriate boundary condition specification on the upstream boundary layer flow. The influence in the resultant wake flow is then evaluated by direct numerical marching of the altered flow into the secondary mixing region. The validity of the porous surface simulation, regarding selected boundary condition equivalence, is evaluated by a complete Navier-Stokes numerical solution for the flow within the immediate slot vicinity. The developed parabolic concepts retain validity for non-separated three-dimensional flows over finite span planar flaps.

The theoretical formulation of the aeroacoustic jet-flap flowfield model is presented. A brief overview of the basic flow illustrates how determined flowfield distributions may be employed in an aeroacoustic model. The required equation sets are presented including appropriate boundary condition specifications as a function of the boundedness of the flow. A finite element algorithm is employed to cast the developed equations in form suitable for direct numerical solution. Results obtained using the COMOC computer program to solve these equations are presented to validate the developed concepts.

SYMBOLS

a	sound speed; boundary condition coefficient
A	Van Driest damping function
c	wall porosity friction factor
C	coefficient
C_f	skin friction
d	differential
e	alternating tensor
f	function of known argument
F	drag force
Fr	Froude number
h	slot nozzle height
H	boundary layer shape factor
I	farfield acoustic intensity
k	turbulence kinetic energy
K	generalized diffusion coefficient
ℓ	differential operator; turbulence length scale
L	differential operator; length
m	finite element index
M	Mach number; number of finite elements spanning R
n	unit normal vector; nodes per element
p	pressure; generalized parameter
P	Stokes stress tensor
q	generalized dependent variable
Q	generalized discretized dependent variable

R	domain of elliptic differential operator
Re	Reynolds number
S	acoustic source term; finite element assembly operator
t	time
T	Lighthill stress tensor
u_i	velocity vector
u, U	reference velocity
u_τ	friction velocity
v, V	scale velocity
x	observer distance
x_i	Cartesian coordinate system
y_i	Cartesian coordinate system
y^+	friction velocity Reynolds number
α	acoustic model parameter
β	acoustic model parameter
∂R	closure of solution domain R
δ	Kronecker delta; boundary layer thickness
δ^*	boundary layer displacement thickness
ϵ	turbulence dissipation function
θ	angle: boundary layer momentum thickness
κ	Karman coefficient (MLT)
λ	multiplier; turbulence sublayer constant (MLT)
μ	dynamic viscosity
ν	kinematic viscosity

ρ	density
σ_{ij}	mean flow Stokes stress tensor
τ_{ij}	Reynolds stress tensor; wall shear stress
ϕ	finite element functional
χ	generalized initial-value coordinate
ψ	streamfunction
ω	turbulence damping factor; frequency; vorticity
Ω	solution domain

Superscripts:

\bullet	effective value
T	matrix transpose
+	turbulence correlation function
\sim	mass-weighted time-average
—	time average
$\hat{}$	unit vector
$\dot{}$	mass-weighted fluctuating component; ordinary derivative
*	approximation

Subscripts:

∞	global reference condition
e	freestream reference condition
i,j,k,l	tensor indices
j	jet reference condition

-	non-tensor index
m	finite element domain
o	initial condition
t	time derivative; turbulent
w	wall reference condition

Notation:

{ }	column matrix
[]	square matrix
\cup	union
\cap	intersection
\in	belongs to

Problem Description

The general configuration for the aeroacoustic flowfield of interest is shown in Fig. 1, illustrating a source of high momentum fluid flowing over an aerodynamic surface subject to acoustic modification. The flow leaves the surface at a sharp trailing edge, tangent to the mean chord, in accordance with the Kutta condition, and proceeds to equilibration with the freestream. It is assumed the flow is essentially unidirectional and parallel to the x_1 (curvilinear) coordinate as shown; hence $u_1 \gg u_2, u_3$, where u_i is the velocity vector.

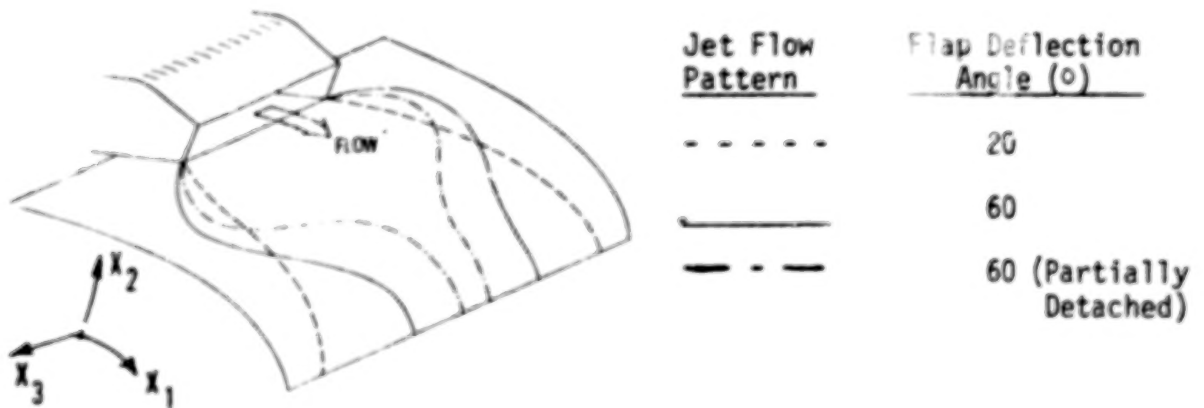


Figure 1. Schematic of Representative Jet Flow Patterns Over Wing/Flap Surface, $M_\infty = 0.8$ (ref. 18)

The point of departure for establishment of an acoustic model is the theory of Lighthill (ref. 2, 3). Based upon an exact analysis using first principles, Lighthill established that the partial differential equation governing propagation of sound in a homogeneous medium at rest is

$$\frac{\partial^2 \rho}{\partial t^2} - a_0^2 \frac{\partial^2 \rho}{\partial x_i^2} = \frac{\partial^2 T_{ij}}{\partial x_i \partial x_j} \quad (1)$$

where a_0 is the reference sound speed, and the solution domain is assumed devoid of solid surfaces. Equation (1) is recognized as the wave equation; it possesses the retarded-time solution, expressed in terms of the perturbation to the mean density at the point x_i , and the source strength distribution at y_i , in the form

$$\rho - \rho_0 = \frac{1}{4\pi a_0^2} \frac{\partial^2}{\partial x_i \partial x_j} \int T_{ij} \left(y, t - \frac{|x - y|}{a_0} \right) \frac{dy}{|x - y|} \quad (2)$$

The noise source mechanisms are described by the Lighthill stress tensor, T_{ij} , the right side of equation (1). They consist of the instantaneous convective accelerations and force terms as

$$T_{ij} = \rho u_i u_j + P_{ij} - a_0^2 \rho \delta_{ij} \quad (3)$$

The P_{ij} tensor contains the pressure and local viscous stresses and is expressed as

$$P_{ij} \equiv p \delta_{ij} + \mu \left[\frac{\partial u_i}{\partial x_j} + \frac{\partial u_j}{\partial x_i} - \frac{2}{3} \frac{\partial u_k}{\partial x_k} \delta_{ij} \right] \quad (4)$$

A useful characterization of the terms in equation (3) is obtained by decomposition of the velocity field into mean time-averaged and fluctuating components as

$$u_i = \bar{u}_i + u'_i \quad (5)$$

Hence,

$$T_{ij} = \rho(\bar{u}_i + u'_i)(\bar{u}_j + u'_j) + P_{ij} - a_0^2 \rho \delta_{ij} \quad (6)$$

Evaluation of the second derivative of equation (6) is required; applying the continuity equation, the instantaneous source term of the acoustic equation in mean velocity field \bar{u}_j is

$$\begin{aligned} S &\equiv \frac{\partial^2 T_{ij}}{\partial x_i \partial x_j} \equiv T_{ij,j i} \\ &= \rho(\bar{u}_{j,i} \bar{u}_{i,j} + \bar{u}_{i,i} \bar{u}_{j,j}) - 2\bar{u}_i \rho_{,i t} + \bar{u}_i \bar{u}_j \rho_{,i j} \\ &\quad + 2\bar{u}_{i,j}(\rho u'_j)_{,i} + 2(\bar{u}_{i,i} \rho u'_j)_{,j} + (\rho u'_i u'_j)_{,i j} \\ &\quad + P_{ij,j i} - a_0^2 \rho_{,j j} \end{aligned} \quad (7)$$

The density derivative terms are removed by a Galilean transformation. For small Mach number, temperature effects may also be neglected, which deletes the last two terms of equation (7). The source term that requires evaluation then becomes, in a moving reference frame

$$S^* = \rho(\tilde{u}_{j,i}\tilde{u}_{i,j} + \tilde{u}_{i,i}\tilde{u}_{j,j}) + 2\tilde{u}_{i,j}(\rho u_j')_{,i} + 2(\tilde{u}_{i,i}\rho u_j')_{,j} + (\rho u_i' u_j')_{,ij} \quad (8)$$

Previous analyses for elementary jet and wake flows have idealized the mixing layer by the assumption that only \tilde{u}_1 is non-vanishing and that it is independent of x_1 . This removes the first and third terms in equation (8) and simplifies the remaining summations. For the jet-flap flows of interest, however, the assumption that $\tilde{u}_1 = \tilde{u}_1(x_2)$ is inappropriate, especially at the flap terminus where large local accelerations can occur. The assumption on transverse mean velocity remains valid, however, which yields

$$S^* \approx 2\tilde{u}_{1,j}(\rho u_j')_{,1} + 2(\tilde{u}_{1,1}\rho u_j')_{,j} + (\rho u_i' u_j')_{,ij} \quad (9)$$

The third term in equation (9) was originally analyzed by Proudman (ref. 23) using an isotropic turbulence model for free jets. The lead term was first identified by Mollo-Christensen & Marasimbo (ref. 24). In the terminology of Lilley (ref. 25) the third term is called the "self noise" due to its quadrupole nature. The first term is called the "shear noise" since the shear components are modified by the mean velocity derivative. The potential importance of the second term stems from the existence of the terminus of the trailing edge, a location experimentally verified to be a strong acoustic source.

Substitution of equation (9) into (2), and utilizing a Galilean space-time transformation, yields the solution expressed in a reference frame moving with the flow as

$$\rho - \rho_0 = \int \left[\frac{x_1}{2\pi a_0^3 M^2} \tilde{u}_{1,j} \frac{\partial}{\partial t} (\rho u_j') + \frac{1}{2\pi a_0^2 M} \tilde{u}_{1,1j} \rho u_j' + \frac{x_j}{2\pi a_0^3 M^2} \tilde{u}_{1,1} \frac{\partial}{\partial t} (\rho u_j') + \frac{x_i x_j}{4\pi a_0^4 M^3} \frac{\partial^2}{\partial t^2} (\rho u_i' u_j') \right] dt \quad (10)$$

The farfield noise intensity has been determined from the variance of equation (10) in a fixed reference frame, as

$$I(x) \equiv \frac{a_0^3}{\rho_0} \overline{[\rho - \rho_0]_i [\rho - \rho_0]_j} \quad (11)$$

The product is understood to include all possible tensor combinations. The overbar indicates time-averaged and equation (11) represents the noise intensity measured at observer location x due to all coherent sources.

Evaluation of integrals in equation (11) is complex; modeling can be employed to express the covariances in terms of correlations of the turbulent flowfield. Equation (11) becomes a single evaluation in a uniform mean flow with isotropic turbulence since only the self-noise term persists. Proudman (ref. 23) evaluated a simplified model using the concept of an eddy volume, beyond which significant coherence vanishes. He established the intensity at a point in the farfield for a moving reference frame as

$$I(x) = \frac{38\rho_0(k)^{5/2}\epsilon|x|^4}{4\pi M_x^6} \quad (12)$$

In equation (12), k is turbulence kinetic energy

$$k = \frac{1}{2} \overline{u_i' u_i'} \quad (13)$$

which for isotropic turbulence is $\overline{u_i' u_i'}$. The turbulence dissipation function ϵ is defined as

$$\epsilon \delta_{ij} \equiv 3\bar{\nu} \frac{\partial u_i'}{\partial x_k} \frac{\partial u_j'}{\partial x_k} \quad (14)$$

where ν is the fluid kinematic viscosity. M_x is an eddy convection factor.

The derivation procedure of Proudman was applied to the mean shear noise term of equation (9) by Lilley (ref. 25). Under the assumption of isotropic turbulence, the farfield intensity is

$$I(x) = C \left(\frac{\partial \tilde{u}_1}{\partial x_2} \right)^6 k \ell^5 \quad (15)$$

where C is a constant and ℓ is a longitudinal turbulence length scale.

Use of the concept for an axisymmetric free jet was proposed by Moon and Zelazny (ref. 26). For this case, the shear noise term, equation (9), is non-vanishing for $j = 2$, and several additional terms result from the summation implied by the repeated subscripts in the self noise term. In the fashion of Lilley (ref. 25) and Csanady (ref. 27), noise was assumed radiated at two dominant frequencies. The time dependence in equation (11) was expressed in terms of these frequencies and appropriate eddy decay length scales.

Applying a directivity term for the free-jet shear layer flow, devised from geometrical acoustics theory (Csanady, ref. 27), and integrating over appropriately defined eddy volumes, the derived form for equation (11) was

$$I = \left[\frac{\beta_{se} \rho^2 \omega_{se}^4 \ell_1 \ell_2 \ell_3 (\overline{u'_1 u'_1})^2}{8\pi^2 |x|^2 \rho_0 a_0^5 [(1 - M_c \cos \theta)^2 + \alpha_{se}^2 M_c^2]^{5/2}} + \left(\frac{\partial \tilde{u}_1}{\partial r} \right)^2 \frac{\beta_{sh} \rho^2 \omega_{sh}^2 \ell_1 \ell_2 \ell_3 \left\{ (\overline{u'_1 u'_r})^2 \cos^4 \theta + (\overline{u'_r u'_r})^2 \sin^2 \theta \cos^2 \theta \right\}}{2\pi^2 |x|^2 \rho_0 a_0^5 [(1 - M_c \cos \theta)^2 + \alpha_{sh}^2 M_c^2]^{3/2}} \right] d\tau \quad (16)$$

The two terms radiate at the self noise and shear noise frequency respectively. The farfield intensity is an integral over the source field modeled in terms of turbulence parameters, i.e., components of the Reynolds stress tensor. For elementary two-dimensional or axisymmetric boundary layer and shear layer flows, the significant shear component of the Reynolds stress can be expressed as (cf., ref. 28, 29)

$$-\overline{u'_1 u'_2} = C k^{1/2} \ell_d \left[\frac{\partial \tilde{u}_1}{\partial x_2} \right] \quad (17)$$

where C is a constant. The dissipation length scale ℓ_d is a function of k and ϵ as

$$\ell_d = k^{3/2} \epsilon^{-1} \quad (18)$$

Substitution of equations (13), (17) and (18) then yields equation (16) an explicit function of the two-dimensional distributions of turbulence correlations and mean flow shear.

The present focus is the more complex attached aerodynamic flow over and downstream of the terminus of a flap with a sharp trailing edge. Added complexity results from \tilde{u}_1 becoming a function of both x_1 and x_2 ; \tilde{u}_2 and \tilde{u}_3 remain negligibly small to first order. Several additional terms may assume importance in equation (9) as the j summations now range over 1 and 2. Hence, both x_1 and x_2 derivatives of \tilde{u}_1 , as well as the turbulence correlations and several cross-product terms would result. A computational study of the basic flow geometry could initially focus on establishing detailed distributions of \tilde{u}_1 and turbulence correlations, for example, k , ϵ and ℓ_d and their derivatives.

The Flowfield Equations

The basic aerodynamic character of the jet-flap flowfield has been illustrated. It is required to establish subsets of the governing Navier-Stokes equations that adequately describe the fundamental flow character and are also amenable to numerical solution. In Cartesian tensor notation, with summation implied for repeated latin subscripts, the non-dimensional form for mass and momentum conservation for flow of a compressible, single-species, isoenergetic perfect fluid is

$$L(\rho) \equiv \frac{\partial \rho}{\partial t} + \frac{\partial}{\partial x_j}(\rho u_j) = 0 \quad (19)$$

$$L(\rho u_i) \equiv \frac{\partial}{\partial t}(\rho u_i) + \frac{\partial}{\partial x_j}[\rho u_j u_i + p \delta_{ij} - Re^{-1} \sigma_{ij}] + Fr^{-1} \rho b_i = 0 \quad (20)$$

The dependent variables in equations (19)-(20) have their usual interpretation in fluid mechanics where ρ is mass density, u_j is the velocity vector, p is the static pressure, b is the body force, Re is the Reynold's number and Fr is the Froude number. The Stokes stress tensor, σ_{ij} is defined in terms of the dynamic viscosity μ as

$$\sigma_{ij} \equiv \mu \left[\frac{\partial u_i}{\partial x_j} + \frac{\partial u_j}{\partial x_i} \right] - \frac{2\mu}{3} \frac{\partial u_k}{\partial x_k} \delta_{ij} \quad (21)$$

The Navier-Stokes system, equations (19)-(21), becomes amenable to numerical solution techniques in a practical sense only after time-averaging. Employing the Reynold's decomposition (cf., ref. 30), define

$$u_i = \tilde{u}_i + u_i' \quad (22)$$

where \tilde{u}_i is the mass-weighted, time-averaged velocity

$$\tilde{u}_i \equiv \frac{\overline{\rho u_i}}{\bar{\rho}} \quad (23)$$

and u_i' are the velocity fluctuations about the mean flow. By definition,

$$\overline{\rho u_i'} = \lim_{T \rightarrow \infty} \frac{1}{T} \int_{t_0}^{t_0+T} (\rho u_i' - \bar{\rho} \tilde{u}_i) dt = 0 \quad (24)$$

and

$$\overline{\rho u_i u_j} = \bar{\rho} \bar{u}_i \bar{u}_j + \overline{\rho u_i' u_j'} \quad (25)$$

The time-averaged equivalent of the Navier-Stokes equations (19)-(20) becomes

$$L(\bar{\rho}) = \frac{\partial \bar{\rho}}{\partial t} + \frac{\partial}{\partial x_j} (\bar{\rho} \bar{u}_j) = 0 \quad (26)$$

$$L(\bar{\rho} \bar{u}_i) = \frac{\partial (\bar{\rho} \bar{u}_i)}{\partial t} + \frac{\partial}{\partial x_j} \left[\bar{\rho} \bar{u}_j \bar{u}_i + \frac{\partial \bar{p}}{\partial x_i} - (\bar{\sigma}_{ij} - \overline{\rho u_i' u_j'}) \right] = 0 \quad (27)$$

where $\bar{\sigma}_{ij}$ is the time-averaged mean flow stress tensor,

$$\bar{\sigma}_{ij} \equiv \frac{\bar{\mu}}{\text{Re}} \left[\frac{\partial \bar{u}_i}{\partial x_j} + \frac{\partial \bar{u}_j}{\partial x_i} - \frac{2}{3} \frac{\partial \bar{u}_k}{\partial x_k} \delta_{ij} \right] \quad (28)$$

In eqn. 28, $\bar{\mu}$ is the time-averaged dynamic viscosity, and the fourth term in the divergence is called the Reynolds stress tensor τ_{ij} .

$$\tau_{ij} \equiv -\overline{\rho u_i' u_j'} \quad (29)$$

We seek approximations to the steady-flow, time-averaged Navier-Stokes equations that yield adequate flowfield descriptions that are economically amenable to numerical solution using present day computers. One simplification is the parabolic approximation which can yield three-dimensional flow descriptions while requiring only two-dimensional computer storage. The three-dimensional parabolic Navier-Stokes equations (3DPNS) describe steady, confined or unbounded, viscous and turbulent flowfields wherein:

- 1) a predominant flow direction is uniformly discernible,
- 2) only in this direction are diffusion processes negligible compared to convection, and,
- 3) no significant flowfield disturbances are propagated upstream against the predominant flow.

Figure 2 illustrates the basic rectangular slot nozzle-planar jet flap configuration of interest, including representation of a finite element discretization and flap surface treatment, which is amenable to flowfield

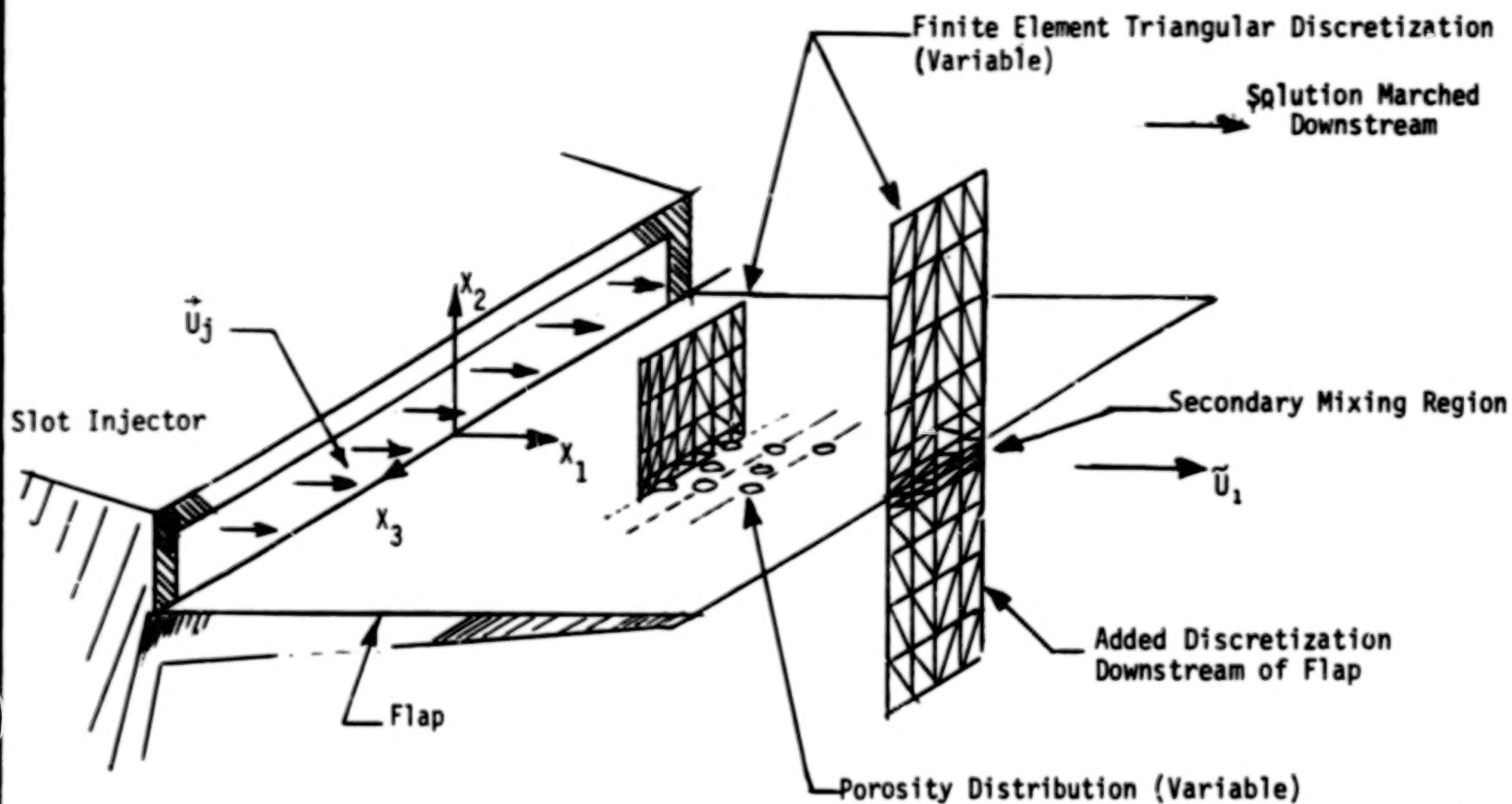


Fig. 2 Three-Dimensional Representation of A Rectangular Slot Injector - Planar Jet Flap Configuration

characterization using the 3DPNS equation system. The predominant direction of flow is assumed parallel to the x_1 coordinate. The parabolic approximation to equations (26)-(28) is accomplished by eliminating diffusion in this direction; hence, equation (28) becomes

$$\bar{\sigma}_{ij} = \frac{\bar{\mu}(1 - \delta_{i1})}{Re} \left[\frac{\partial \bar{u}_i}{\partial x_j} + \frac{\partial \bar{u}_j}{\partial x_i} - \frac{2}{3} \frac{\partial \bar{u}_k}{\partial x_k} \delta_{ij} \right] \quad (30)$$

The mean flow unidirectionality assumption will also affect terms retained in the Reynold's stress model, as discussed in the next section. The subscript bar notation denotes the index not eligible for summation, but is synonymous with the identical tensor index.

The 3DPNS equation system contains, as a subset, the familiar two-dimensional boundary layer (2DBL) and two-dimensional parabolic Navier-Stokes (2DPNS) equations. Both these systems are employed to predict the jet-flap flow evolution on the symmetry plane of the three-dimensional geometry illustrated in Figure 2. The two-dimensional geometry is illustrated in Figure 3, including labeling of the primary and secondary mixing regions. For illustration, the 2DPNS equations in expanded form are

$$L(\bar{p}) = \frac{\partial(\bar{p}\bar{u}_1)}{\partial x_1} + \frac{\partial(\bar{p}\bar{u}_2)}{\partial x_2} = 0 \quad (31)$$

$$\begin{aligned} L(\bar{p}\bar{u}_1) = & \bar{p}\bar{u}_1 \frac{\partial \bar{u}_1}{\partial x_1} + \bar{p}\bar{u}_2 \frac{\partial \bar{u}_1}{\partial x_2} + \frac{\partial \bar{p}}{\partial x_1} - \frac{1}{Re} \frac{\partial}{\partial x_2} \left[\bar{\mu} \frac{\partial \bar{u}_1}{\partial x_2} \right] \\ & - \frac{\partial}{\partial x_1} \left[\overline{-\rho u_1' u_1'} \right] - \frac{\partial}{\partial x_2} \left[\overline{-\rho u_1' u_2'} \right] = 0 \end{aligned} \quad (32)$$

$$\begin{aligned} L(\bar{p}\bar{u}_2) = & \bar{p}\bar{u}_1 \frac{\partial \bar{u}_2}{\partial x_1} + \bar{p}\bar{u}_2 \frac{\partial \bar{u}_2}{\partial x_2} + \frac{\partial \bar{p}}{\partial x_2} - \frac{1}{Re} \frac{\partial}{\partial x_2} \left[\bar{\mu} \frac{\partial \bar{u}_2}{\partial x_2} \right] \\ & - \frac{\partial}{\partial x_1} \left[\overline{-\rho u_1' u_2'} \right] - \frac{\partial}{\partial x_2} \left[\overline{-\rho u_2' u_2'} \right] = 0 \end{aligned} \quad (33)$$

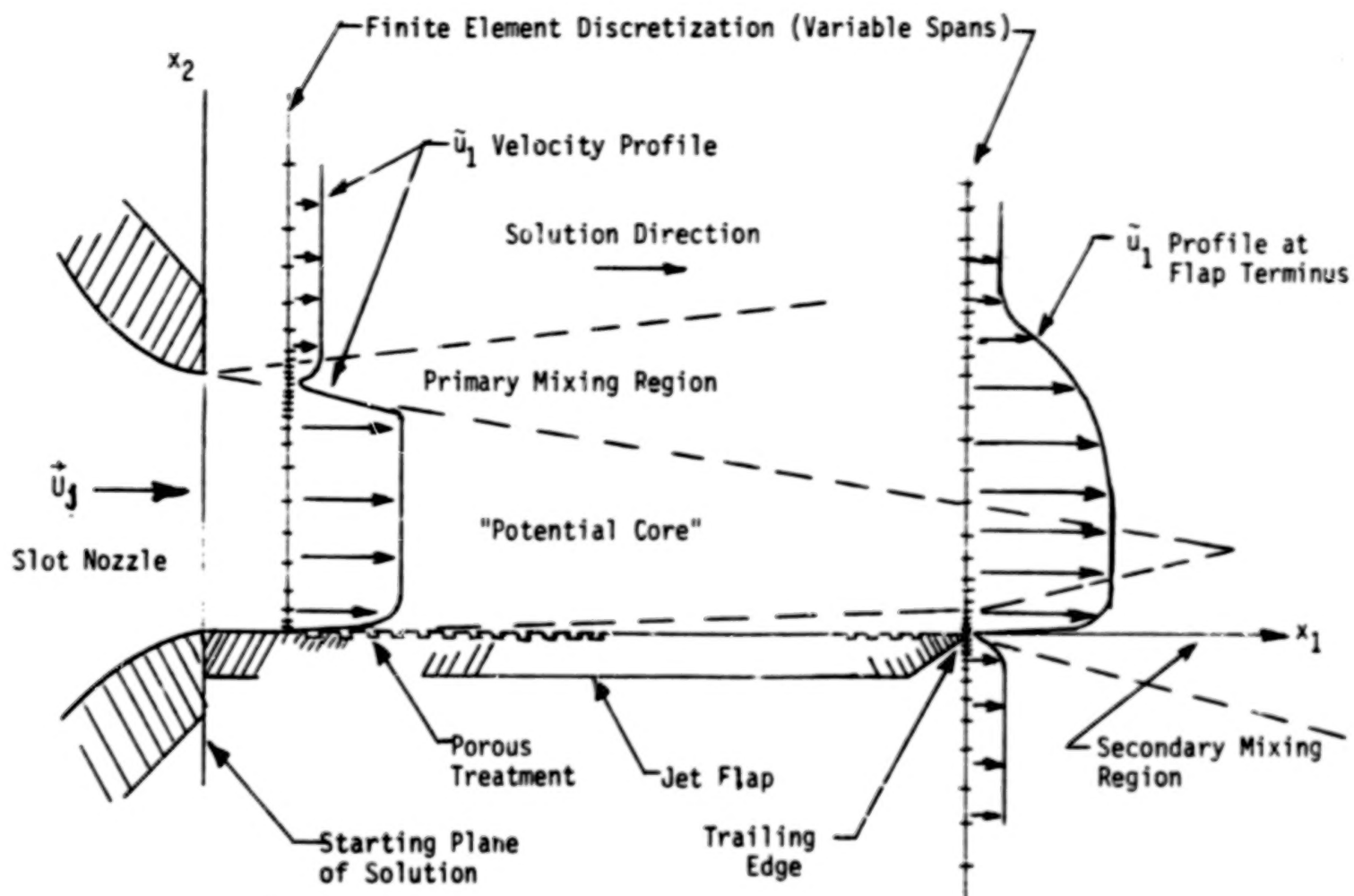


Fig. 3 Two-Dimensional Symmetry Plane Flowfield For Rectangular Slot Nozzle - Planar Jet Flap Configuration

The dependent variables in the 3DPNS and 2DPNS system are the mean steady flow vector \bar{u}_i and pressure \bar{p} . For a two-dimensional boundary layer, the x_1 pressure gradient is known from the freestream flow, and impressed across the boundary layer thickness. According to the same order of magnitude analysis, equation (33) vanishes identically to first order, yielding a second-order balancing of perturbation in pressure to the Reynolds stress normal component as

$$L(p) = \frac{\partial}{\partial x_2} \left[\bar{p} + \overline{\rho u_2' u_2'} \right] = 0 \quad (34)$$

Closure of the 3DPNS system requires specification of τ_{ij} ; the turbulence model is discussed in the next section.

The essential differential character of the 3DPNS momentum equation is initial-value in the x_1 coordinate and boundary value on the (x_2, x_3) plane. Hence, given an initial distribution of \bar{u}_i , equations (27)-(28) are marched downstream parallel to x_1 , and boundary conditions are imposed on the flap surface and at all lateral locations whereat the viscous jet flow merges with the assumed inviscid freestream. The starting solution plane and the location of boundary conditions specification is denoted in Figure 3 for the two-dimensional case. The boundary condition location for a three-dimensional case occurs everywhere along the outer extremity of the finite element grid illustrated in Figure 2. Correspondingly, on this closure segment, the jet velocity asymptotically matches the freestream value which is enforced as a gradient boundary condition. The velocity vector vanishes identically on the flap surface segment, Fig. 2-3, except if the flap is assumed porous, whereupon \bar{u}_2 takes on a specified non-zero value, i.e., $\bar{u}_i(x_1, 0, x_3) \equiv V_w(x_1, x_3)$. For the planar flap symmetry plane cases studied, the freestream pressure is uniform; therefore, to first order, the pressure is everywhere constant, and equation (34) provides a second-order estimate of pressure variation. The continuity equation (31) provides the freestream boundary condition for solution of equation (33) for transverse velocity in the secondary mixing region. For the boundary layer solution on the flap surface, equation (31) is solved directly for \bar{u}_2 as an initial-value problem in the x_2 coordinate direction. Hence, a complete jet-flap flowfield solution requires a switching of equation solution procedure as the flow departs the flap trailing edge.

The second simplification applied to the time-averaged steady-flow Navier-Stokes equations (26)-(28), for evaluation of a porous jet-flap flow, is reduction to two-dimensional space and transformation of dependent variables to a vorticity-streamfunction description (cf., ref. 31). In subsonic flows for which density may be assumed constant, equation (26) defines a divergence-free field, $\bar{\rho} \bar{u}_i$. From vector field theory, an equivalent expression on spaces spanned by Cartesian coordinates is

$$\bar{\rho} \bar{u}_i \equiv J^{-1} \epsilon_{ijk} \frac{\partial \psi_k}{\partial x_j} \quad (35)$$

where e_{ijk} is the alternating tensor, J is the determinant of the metric, and ψ_k is the streamfunction vector. Substitution of equation (35) into (26) yields an identity in zero. A useful transformation of equation (27) is accomplished by definition of the vorticity vector

$$\omega_i \equiv \frac{1}{J} e_{ijk} \frac{\partial \tilde{u}_k}{\partial x_j} \quad (36)$$

For two-dimensional problems, the sole non-vanishing scalar components for both ψ_k and ω_k correspond to $k = 3$, in which case an elementary 2DNS differential equation set can be established. Denoting the x_i components of ψ_k and ω_k as ψ and ω , respectively, the compatibility equation results from substitution of equation (35) into (36) yielding,

$$L(\psi) = \frac{\partial}{\partial x_j} \left[\frac{1}{\bar{\rho}} \frac{\partial \psi}{\partial x_j} \right] + \omega = 0 \quad (37)$$

Taking the curl of equation (27) to eliminate the pressure and substituting equations (35)-(36), yields the two-dimensional vorticity transport equation (cf., ref. 31),

$$L(\omega) = \bar{\rho} \frac{\partial \omega}{\partial t} + e_{3ki} \frac{\partial}{\partial x_k} \left[\omega \frac{\partial \psi}{\partial x_i} + \frac{\partial}{\partial x_j} (\bar{\sigma}_{ij} - \bar{\rho} u_i' u_j') \right] = 0 \quad (38)$$

where $\bar{\sigma}_{ij}$ is defined by equation (28).

Equations (37)-(38) can be employed to evaluate two-dimensional transient low speed aeroacoustic flows wherein separation and recirculation are dominant features. Their use is appropriate, for example, for a detailed analysis of the flow departing a blunt trailing edge of a jet flap. For the present study, this equation set was solved for the recirculating flow within the immediate vicinity of a simulated porous slot on the jet flap surface, see Figure 3. The solution domain is shown in Figure 4, along with a representative finite element discretization.

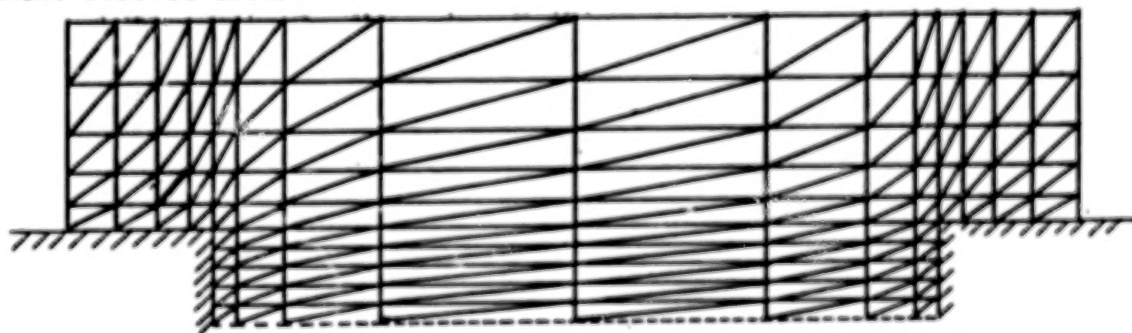


Fig. 4 Porous Slot Flow Solution Domain

Flow enters from the left, and the base of the slot region is assumed porous, hence a source or sink for mass. Equations (37)-(38) are both boundary value problem descriptions, hence boundary condition specification is appropriate about the entire closure illustrated in Figure 4. Any specified inlet/outlet velocity defines both ψ and ω , using equations (35)-(36). Along the solid flap surface, ψ is a constant and the no-slip boundary condition equivalent for ω is (cf., ref. 31)

$$\omega_w = -\frac{1}{\bar{\rho}} \frac{d^2 \psi}{dx_n^2} \quad (39)$$

where x_n is the coordinate normal to the wall. Since equation (38) is also initial-value, the initial vorticity contour ω_0 is determined from a specified velocity distribution using equation (36). The initial distribution for ψ is obtained from solution of equation (37) using ω_0 .

The identified partial differential equations systems are potentially useful for determination of the turbulent aeroacoustic flowfields characteristic of the basic jet-flap geometry. It remains to establish a closure model for turbulence phenomena, to allow determination of the Reynolds stress tensor in terms of computational variables.

Turbulence Closure Modeling

The operation of time-averaging has introduced the Reynolds stress into the Navier-Stokes equations as well as the simplified subsystems identified for analysis of the jet flap flowfield. The primary requirement is for development of a closure model for the steady flow parabolic approximation, since the presented full Navier-Stokes analyses are restricted to flows dominated by wall damping. Using well known procedures (cf., ref. 32), the exact partial differential equation description for the kinematic Reynolds stress $-u_i' u_j'$ in a steady mean flow is

$$\begin{aligned} L(u_i' u_j') &= \frac{\partial}{\partial x_k} (\bar{u}_k' \bar{u}_i' u_j') + \left[\bar{u}_j' u_k' \frac{\partial \bar{u}_i'}{\partial x_k} + \bar{u}_i' u_k' \frac{\partial \bar{u}_j'}{\partial x_k} \right] \\ &+ 2\bar{\nu} \frac{\partial \bar{u}_i' \partial \bar{u}_j'}{\partial x_k \partial x_k} + \frac{\bar{p}}{\rho} \left[\frac{\partial \bar{u}_i'}{\partial x_j} + \frac{\partial \bar{u}_j'}{\partial x_i} \right] \\ &+ \frac{\partial}{\partial x_k} \left[\bar{u}_i' u_j' u_k' - \bar{\nu} \frac{\partial \bar{u}_i' u_j'}{\partial x_k} + \frac{\bar{p}}{\rho} (\delta_{jk} \bar{u}_i' + \delta_{ik} \bar{u}_j') \right] = 0 \end{aligned} \quad (40)$$

where $\bar{\nu}$ is the kinematic viscosity, $\bar{\mu}/\bar{\rho}$.

Equation (40) is the departure point for development of a closure model. An additional differential equation for turbulence dissipation rate ϵ is required; assuming the process is isotropic,

$$\frac{2}{3}\delta_{ij}\epsilon \equiv 2\bar{v} \frac{\partial u_i' \partial u_j'}{\partial x_k \partial x_k} \quad (41)$$

The exact transport equation for dissipation function ϵ is (cf., ref. 30).

$$\begin{aligned} L(\epsilon) = & \frac{\partial}{\partial x_k} (\bar{u}_k \epsilon) + 2\bar{v} \frac{\partial u_i'}{\partial x_k} \frac{\partial u_i'}{\partial x_l} \frac{\partial u_k'}{\partial x_l} + 2 \left[\bar{v} \frac{\partial^2 u_i'}{\partial x_k \partial x_l} \right]^2 \\ & + \frac{\partial}{\partial x_k} \left[\bar{v} u_k' \frac{\partial u_i'}{\partial x_l} \frac{\partial u_i'}{\partial x_l} + \frac{v}{\rho} \frac{\partial p}{\partial x_i} \frac{\partial u_k'}{\partial x_i} \right] = 0 \end{aligned} \quad (42)$$

Equations (40)-(42) represent seven additional partial differential equations describing turbulence phenomena. However, this system is not closed since the third order correlations remain undefined. Additional differential equations could be established, but they in turn would involve undefined fourth order terms. Hence, modeling of third order correlations is invoked at a level of completeness, dependent upon the dimensionality and geometrical complexity of the physical system. For example, Launder et al (ref. 33) present closure in terms of all components of $-u_i' u_j'$. They document validity of the model for several cases including isotropic turbulence, free shear flows, elementary duct flows and flat plate boundary layer flows.

In earlier work, Hanjalic' and Launder (ref. 29), establish a closure applicable to thin shear flows where in only $-u_1' u_2'$ is retained, and solved in combination with ϵ and the turbulence kinetic energy k defined as

$$k \equiv \frac{1}{2} \overline{u_i' u_i'} \quad (43)$$

For the uni-directional, shear-dominated flows of primary interest, wherein $\bar{u}_1 \gg \bar{u}_2, \bar{u}_3$, the contraction of equation (40) yields, after application of the parabolic approximation,

$$\begin{aligned} L(k) = & \frac{\partial}{\partial x_j} (\bar{u}_j k) - C_k \frac{\partial}{\partial x_l} \left[k^2 \epsilon^{-1} \frac{\partial k}{\partial x_l} \right] \\ & - \overline{u_1' u_l'} \frac{\partial \bar{u}_1}{\partial x_l} + \epsilon = 0 \end{aligned} \quad (44)$$

Equation (44) defines a new summation index convention appropriate for 3DPNS as, $1 \leq i, j \leq 3$ and $2 \leq l \leq 3$. The corresponding form for the dissipation equation (42) is

$$\begin{aligned} L(\epsilon) = & \frac{\partial}{\partial x_j} (\bar{u}_j \epsilon) - C_\epsilon \frac{\partial}{\partial x_i} \left[k \epsilon^{-1} \overline{u_i' u_j'} \frac{\partial \epsilon}{\partial x_j} \right] \\ & - C_\epsilon^1 \overline{u_1' u_l'} \epsilon k^{-1} \frac{\partial \bar{u}_l}{\partial x_l} + C_\epsilon^2 \epsilon^2 k^{-1} = 0 \end{aligned} \quad (45)$$

In equations (44)-(45), the various constants C_α are determined from approximate analyses and/or computer optimization (ref. 33).

The next level of simplification involves specification of an effective turbulent diffusion coefficient ν_t . From first principles (cf., ref. 32), the effective diffusion coefficient must be of the form

$$\nu_t \equiv C V l \quad (46)$$

where C is a constant, V a scale velocity, and l a scale length. For the turbulence kinetic energy-dissipation function two equation closure hypothesis (herein named TKE), V is taken as the square root of turbulence kinetic energy, equation (43). A dissipation length scale l_d defined in terms of k and ϵ (ref. 34) is,

$$l_d \equiv k^{3/2} \epsilon^{-1} \quad (47)$$

The TKE closure hypothesis then specifies

$$\nu_t = C_\nu k^2 \epsilon^{-1} \quad (48)$$

Note that this is precisely the diffusion coefficient for turbulent kinetic energy, equation (44). Furthermore, upon summing the diffusion terms in equation (45), using equation (43) and assuming isotropy, equation (48) yields the diffusion coefficient for dissipation function as well.

To close the 3DPNS mean flow system, it is also required to model the correlation between the shear components of the Reynold's stress tensor and k , ϵ and the mean velocity field \bar{u}_i . Viewing equation (30), and neglecting dilution, the required relation is assumed of the form

$$-\overline{u'_i u'_l} \equiv C_{i\bar{l}} k^2 \epsilon^{-1} \left[\frac{\partial \bar{u}_i}{\partial x_l} + \frac{\partial \bar{u}_l}{\partial x_i} \right] \quad (49)$$

The subscript bar indicates the index not eligible for summation. The elements of the correlation tensor $C_{i\bar{l}}$ are determined from a simplified analysis or experiment; the index range is restricted under the parabolic assumption.

For the analysis reported herein, the 2DPNS and 3DPNS equation systems are closed assuming that $C_{i\bar{l}}$ in equation (49) is a diagonal tensor. The overall effective diffusion coefficient can then be written as

$$\mu^e \equiv \frac{1}{Re} \bar{\mu} + \bar{\rho} \nu_t \quad (50)$$

The 3DPNS equation system for steady mean flow and turbulence closure, using the defined two-equation model and effective diffusion coefficient, then becomes

$$L(\bar{\rho}) = \frac{\partial}{\partial x_j} (\bar{\rho} \bar{u}_j) = 0 \quad (51)$$

$$L(\bar{u}_i) = \frac{\partial}{\partial x_j} (\bar{\rho} \bar{u}_j \bar{u}_i) - \frac{\partial}{\partial x_l} \left[\mu^e \left(\frac{\partial \bar{u}_i}{\partial x_l} + \frac{\partial \bar{u}_l}{\partial x_i} \right) \right] + \frac{\partial \bar{p}}{\partial x_i} = 0 \quad (52)$$

$$L(k) = \frac{\partial}{\partial x_j} (\bar{\rho} \bar{u}_j k) - \frac{\partial}{\partial x_l} \left[\frac{\mu^e}{Pr_k} \frac{\partial k}{\partial x_l} \right] - \mu^e \frac{\partial \bar{u}_1}{\partial x_l} \frac{\partial \bar{u}_1}{\partial x_l} + \rho \epsilon = 0 \quad (53)$$

$$L(\epsilon) = \frac{\partial}{\partial x_j} (\bar{\rho} \bar{u}_j \epsilon) - \frac{\partial}{\partial x_l} \left[\frac{\mu^e}{Pr_\epsilon} \frac{\partial \epsilon}{\partial x_l} \right] - C_\epsilon^1 \epsilon k^{-1} \mu^e \frac{\partial \bar{u}_1}{\partial x_l} \frac{\partial \bar{u}_1}{\partial x_l} + C_\epsilon^2 \rho \epsilon^2 k^{-1} = 0 \quad (54)$$

The tensor indices range $1 \leq i, j \leq 3$ and $2 \leq \ell \leq 3$ for 3DPNS. For symmetry plane analyses using 2DPNS, $1 \leq i, j \leq 2$, $\ell = 2$ only. Hence, since $i = 1$ corresponds to the direction of predominant flow, diffusion is restricted to the plane transverse to the x_1 coordinate, as required by the parabolic assumption. The recommended values for correlation coefficients for shear layer flows are given in Table 1 (cf., ref. 33, 34).

Table 1
Coefficients in TKE Closure Model

Variable	Equation No.	Coefficients
ν_t	(48)	$C_\nu = 0.09$
k	(53)	$Pr_k = 1.0$
ϵ	(54)	$Pr_\epsilon = 1.3, C_\epsilon^1 = 1.44, C_\epsilon^2 = 1.92$

The boundary conditions for the mean flow equations have been described. Since the TKE equations (53)-(54) are also initial-boundary value descriptions, it is necessary to establish appropriate statements. Referring to Figure 3 for example, the levels of k and ϵ vanish in the non-turbulent freestream flow. Since the Reynolds stress hypothesis is valid only in regions where the turbulent Reynolds number is large, it is not economically feasible to enforce k and ϵ to vanish at the flap surface. The alternative selected for these studies is to use boundary layer mixing length concepts to determine the distributions of k and ϵ near the wall. Mixing length theory (MLT) expresses the correlation in equation (46) in terms of the predominant mean flow gradient and a length scale ℓ (ref. 35),

$$\nu_t \equiv \omega^2 \ell^2 \left| \frac{\partial \tilde{u}_1}{\partial x_2} \right| \quad (55)$$

where ℓ is the mixing length

$$\ell \equiv \begin{cases} \kappa x_2 & 0 \leq x_2 \leq \lambda \delta \kappa^{-1} \\ \lambda \delta & x_2 > \lambda \delta \kappa^{-1} \end{cases} \quad (56)$$

and ω is the Van Driest function that accounts for the wall influence on velocity fluctuations.

$$\omega \equiv 1 - \exp(-x_2 A^{-1}) \quad (57)$$

In equation (56), x_2 is the coordinate normal to the flap, δ is the boundary layer thickness, and λ and κ are constants (0.09 and 0.435 respectively). In equation (57), A is a function of many factors influencing flow phenomena near the surface including axial pressure gradient and normal mass flow addition. The form of Cebeci and Smith (ref. 32) serves to unify the many formulations as

$$A \equiv A^+ N^{-1} \left(\frac{\tau_w}{\rho_w} \right)^{-\frac{1}{2}} \left(\frac{\rho}{\rho_w} \right)^{\frac{1}{2}} \quad (58)$$

where

$$N^2 \equiv \frac{v}{v_e} \left(\frac{\rho_e}{\rho_w} \right)^2 \frac{p^+}{v^+} \left[1 - \exp \left(11.8 \frac{v_w}{v} v^+ \right) \right] + \exp \left[11.8 \left(\frac{v_w}{v} \right) v^+ \right] \quad (59)$$

All variables are time-averaged steady components, subscripts e and w refer to freestream and wall values respectively, A^+ is a constant (25.3), and τ_w is the skin friction. Pressure gradient and mass addition effects are accounted for accordingly as

$$p^+ \equiv \left(\frac{v_e \tilde{u}_{1e}}{\tilde{u}_\tau^3} \right) \frac{d\tilde{u}_{1e}}{dx_1} \quad (60)$$

$$v^+ \equiv u_\tau^{-1} v_w \quad (61)$$

where u_e is the freestream axial velocity, v_w is the specified transverse wall velocity, and u_τ is the shear velocity

$$u_\tau \equiv \left(\frac{\tau_w}{\rho} \right)^{\frac{1}{2}} \quad (62)$$

The shear stress, τ_w is defined as

$$\tau_w \equiv \rho_w v_w \left. \frac{\partial \tilde{u}_1}{\partial x_2} \right|_w \quad (63)$$

The Ludwig-Tillman formula (ref. 36) yields

$$\tau_w = \frac{1}{2} \rho_e \bar{u}_{1e}^2 \left[0.246(10)^{-0.678H} Re_\theta^{-0.268} \right] \quad (64)$$

where Re_θ is the Reynolds number based on boundary layer momentum thickness, and $H \equiv \delta^* \theta^{-1}$ where δ^* is the displacement thickness (cf., ref. 35).

Equations (55)-(64) provide the formalisms necessary to determine k and ϵ near a solid surface. These same concepts are employed to complete turbulence closure for the two-dimensional Navier-Stokes solutions for the pore slot recirculating flow, by identifying for equation (38) (cf., ref. 31), where μ^e is given by equations (50) and (55).

$$e_{3ki} \frac{\partial}{\partial x_k} \left[\frac{\partial}{\partial x_j} \left[\bar{\sigma}_{ij} - \overline{\rho u_i' u_j'} \right] \right] \equiv \frac{\partial}{\partial x_k} \left[\mu^e \frac{\partial \omega}{\partial x_k} - \omega \frac{\partial \mu^e}{\partial x_k} \right] \quad (65)$$

Furthermore, through the dual definitions of turbulent effective viscosity, equations (48) and (55), and since the latter involves functions only of the mean axial velocity component \bar{u}_1 , which is either known or readily initialized, a means is established to initialize distributions of both k and ϵ at the node points of a discretization. Since the developed TKE partial differential equations are initial-value, this information is required to start a solution. Additional comments on verification of this procedure are presented in the Appendix.

The closure for turbulence phenomena is complete at the level of sophistication selected for these studies. The partial differential equations governing the flowfields of interest are now closed. All boundary conditions have been appropriately identified for partially and completely unbounded solution domains. The initial-valued character has been noted, and means established to initialize required distributions in terms of readily available data. Numerical solution of the developed system can provide the detailed distributions of mean flow and velocity fluctuation correlations required for a theoretical analysis. It remains to establish the numerical solution algorithm for these equations.

FINITE ELEMENT SOLUTION ALGORITHM

The desired form of the various partial differential equation systems governing the aeroacoustic jet-flap flows of interest are developed. Each is a special case of the general, second-order non-linear elliptic boundary value partial differential equation

$$L(q) = \frac{\partial}{\partial x_\ell} \left[K \frac{\partial q}{\partial x_\ell} \right] + f_1 \left(q, \frac{\partial q}{\partial x_k}, p, x_i \right) + f_2 \left(\bar{u}_1, \frac{\partial q}{\partial x} \right) = 0 \quad (66)$$

Herein, q is the generalized dependent variable, the tensor indices range $2 \leq k, l \leq 3$ and $1 \leq i \leq 3$, K is the diffusion coefficient, f_1 is a function of its argument that specifically includes three-dimensional convection, p is a generalized solution parameter, and f_2 is the initial-value operator. The boundary condition statements for each of the dependent variables can be concisely expressed in the form

$$L(q) = a^{(1)}q + a^{(2)}K \frac{\partial q}{\partial x_l} \hat{n}_l + a^{(3)} = 0 \quad (67)$$

i.e., the normal derivative of q is constrained by q and a parameter as determined by specification of the $a(i)$. An initial condition is required for q identified with each dependent variable as,

$$q(\chi(0), x_2, x_3) \equiv q_0(x_2, x_3) \quad (68)$$

The finite element solution algorithm is based upon the assumption that $L(q)$ is uniformly parabolic within a bounded open domain Ω ; that is, the lead term in equation (66) is uniformly elliptic within its domain R , with closure ∂R , where

$$\Omega \equiv R \times [\chi_0, \chi] \quad (69)$$

and $\chi_0 \leq \chi$. For the 3DPNS equations, χ is associated with the x_1 coordinate. For 2DPNS, it is time. Equation (67) expresses functional constraints on the closure of $\Omega, \partial\Omega \equiv \partial R \times [\chi_0, \chi]$, and the initial-condition specification, equation (68), lies on $R \cup \partial R \times \chi_0$.

The concept of the finite element algorithm involves the assumption that each three-dimensional dependent variable is separable in the form

$$q^*(\chi, x_l) = q_1(\chi) q_l(x_2, x_3) \quad (70)$$

The functional dependence in $q_2(x_2, x_3)$ is represented by a polynomial in x_l . The expansion coefficients q_1 can be most conveniently expressed in terms of the value of $q^*(\chi, x_l)$ at the nodes of the finite element discretization of R . Then, equation (70) takes the form

$$\begin{aligned} q_m^*(\chi, x_l) &= \phi_1(x_l) Q_1(\chi) + \phi_2(x_l) Q_2(\chi) + \phi_3(x_l) Q_3(\chi) \\ &\equiv \{\phi(x_l)\}^T \{Q(\chi)\}_m \end{aligned} \quad (71)$$

where the polynomials $\phi(x_\ell)$ are known functions of x_2 and x_3 . Since they are known, they can be differentiated analytically, e.g.,

$$\frac{\partial q_m^*}{\partial x_2} = \frac{\partial}{\partial x_2} \left\{ \{\phi(x_\ell)\}^T \right\} \{Q(\chi)\}_m \quad (72)$$

Hence, there is no need to establish difference formulae to approximate the differentiated terms in $L(q)$.

The finite element solution algorithm is established for the equation system (66)-(68) using the method of weighted residuals (MWR) formulated on a local basis. Since equation (66) is valid throughout Ω , it is valid within disjoint interior subdomains Ω_m described by $(x_i, \chi) \in R_m \times [\chi_0, \chi]$, called finite elements, wherein $\cup R_m = R$. The approximate solution for q within $R_m \times [\chi_0, \chi]$, called $q_m^*(x_i, \chi)$, is given in equation (71). Therein, the functionals $\phi_k(x_\ell)$ are subsets of a function set that is complete on R_m . The expansion coefficients $Q_k(\chi)$ represent the unknown χ -dependent values of $q_m^*(x_i, \chi)$ at specific locations interior to R and on the closure ∂R_m , called nodes of the finite element discretization of R .

To establish the values taken by these expansion coefficients, require that the local error in the approximate solution to both the differential equation $L(q_m^*)$ and the boundary condition statement $\ell(q^*)$ for $\partial R_m \cap \partial R \neq \emptyset$, be rendered orthogonal to the space of the approximation functions. Employing an algebraic multiplier λ , the resultant equation sets can be combined as

$$S_m \left[\int_{R_m} \{\phi(x_\ell)\} L(q_m^*) d\tau - \lambda \int_{\partial R_m \cap \partial R} \{\phi(x_\ell)\} \ell(q_m^*) d\tau \right] \equiv \{0\} \quad (73)$$

where S_m is the mapping function from the finite element subspace R_m to the global domain R , commonly termed the assembly operator. The number of equations (73) prior to assembly is identical with the number of node points of the finite element R_m .

Equation (73) forms the basic operation of the finite element solution algorithm and of the COMOC computer program to be described. The lead term can be rearranged, and λ determined by means of a Green-Gauss theorem:

$$\begin{aligned} \int_{R_m} \{\phi(x_\ell)\} \frac{\partial}{\partial x_\ell} \left[K \frac{\partial q_m^*}{\partial x_\ell} \right] d\tau &= \oint_{\partial R_m} \{\phi(x_\ell)\} K \frac{\partial q_m^*}{\partial x_\ell} \hat{n}_\ell d\tau \\ &- \int_{R_m} \frac{\partial}{\partial x_\ell} \{\phi(x_\ell)\} K \frac{\partial q_m^*}{\partial x_\ell} d\tau \end{aligned} \quad (74)$$

For $\partial R_m \cap \partial R$ nonvanishing in equation (74), the corresponding segment of the closed-surface integral will cancel the boundary condition contribution, equation (73) by identifying $\lambda a^{(2)}$ with K , equation (66). The contributions to the closed-surface integral, equation (74) whereat $\partial R_m \cap \partial R = 0$, can also be made to vanish. The globally assembled finite-element solution algorithm for the representative partial differential equation system then becomes

$$S_m \left[- \int_{R_m} \frac{\partial}{\partial x_\ell} \{ \phi \} K \frac{\partial q^*}{\partial x_\ell} d\tau + \int_{R_m} \{ \phi \} (f_1^* + f_2^*) d\tau - \int_{\partial R_m \cap \partial R} \{ \phi \} [a^{(1)} q^* + a^{(3)}] d\tau \right] \equiv \{ 0 \} \quad (75)$$

The rank of the global equation system (75) is identical with the total number of node points on $R \cup \partial R$ for which the dependent variable requires solution. Equation (75) is a first-order, ordinary differential system for 3DPNS. For streamfunction in 2DNS, it is algebraic and the matrix structure is sparse and banded. Solution of the initial-value system is obtained by COMOC using a predictor-corrector finite-difference numerical integration algorithm. A banded Cholesky equation solver is employed to solve an algebraic equation.

Solution is also required for the continuity equation (48) which is retained for boundary-layer flows. Since it exists in standard form as an ordinary differential equation, direct numerical integration yields the required solution at node points of the discretization.

COMOC COMPUTER PROGRAM

The finite element solution algorithm is utilized, as observed in the previous section, to cast the original initial-valued, elliptic boundary-value problem description into large-order systems of purely initial-value and/or boundary value problems. The COMOC computer program system is being developed to transmit the rapid theoretical progress in finite element solution methodology into a viable numerical solution capability. COMOC integrates or equation-solves the discretized equivalent of the governing equation system. Initial distributions of all dependent variables may be appropriately specified or computed, and boundary constraints for each dependent variable can be specified on arbitrarily disjoint segments of the solution domain closure. The solutions for each dependent variable, and all computed parameters, are established at node points lying on a specifiably nonregular computational lattice, formed by plane triangulation of the elliptic portion of the solution domain Ω , i.e., $RU \cup R$.

The COMOC system is built upon the macrostructure illustrated in Figure 5. The Main executive routine allocates core, using a variable dimensioning scheme, based upon the total degrees of freedom of the global problem statement. The size of the largest problem that can be solved is thus limited (only) by the available core of the computer in use. The precise mix between dependent variables and parameters, and fineness of the discretization, is user-specifiable and widely variable. The Input module serves its standard function for all arrays of dependent variables, parameters, and geometric coordinates. The Discretization module forms the finite-element discretization of the elliptic solution domain and evaluates all required finite-element nonstandard matrices and standard-matrix multipliers. The Initialization module computes the remaining initial parametric data required to start the solution. The Integration module constitutes the primary execution sequence of problem solution, and utilizes a highly stable, predictor-corrector integration algorithm for the column vector of unknowns of the solution. Calls to auxiliary routines for parameter evaluation (effective viscosity, Prandtl number, source terms, etc.) as specified functions of dependent and/or independent variables, as well as calls for equation solving algebraic systems, are governed by the Integration module. The Output module is similarly addressed from the integration sequence and serves its standard function via a highly automated array-display algorithm. COMOC can execute distinct problems in sequence, and contains an automatic restart capability to continue solutions. A discussion on the functional design of COMOC is given in reference 37.

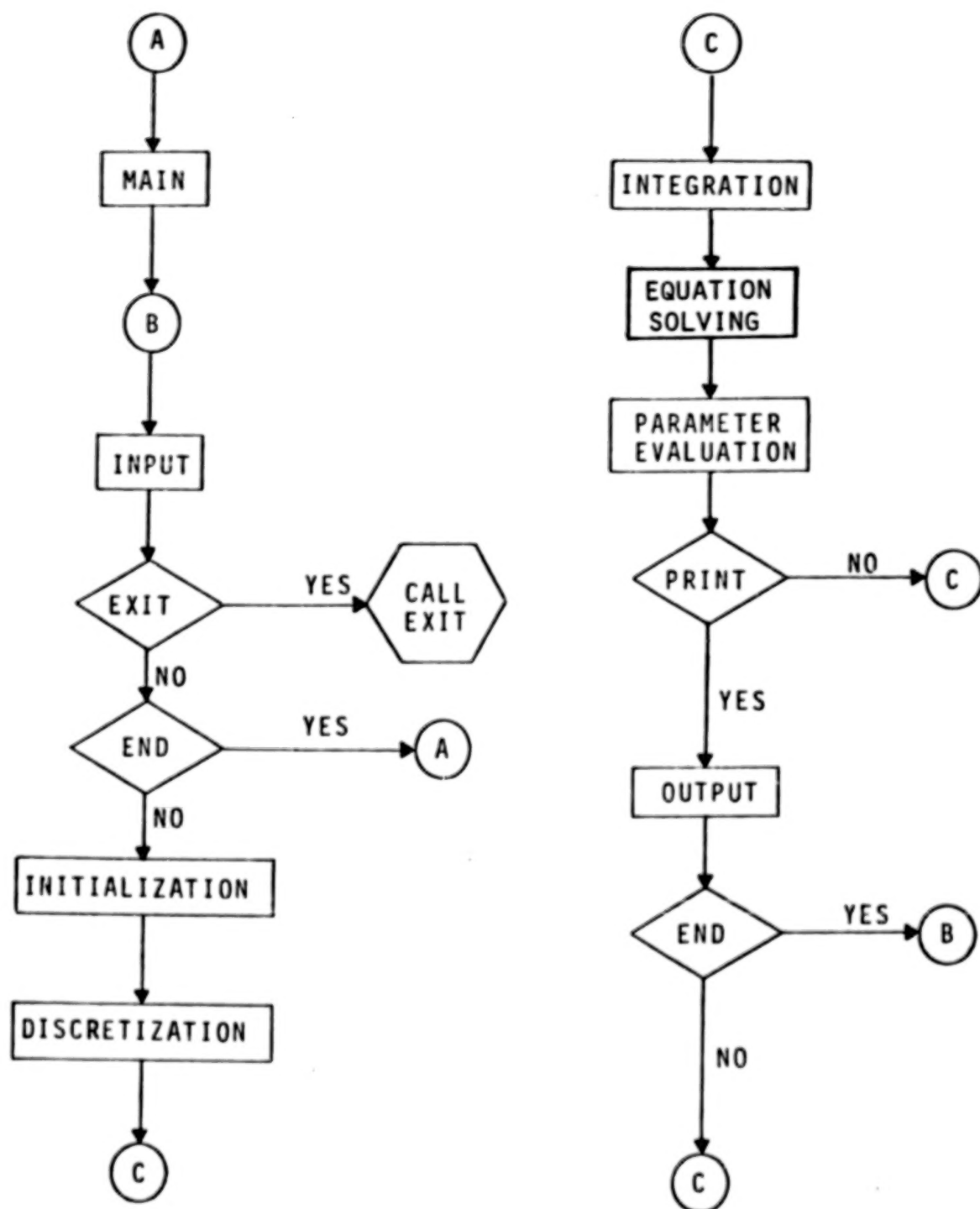


Figure 5 COMOC Macro-structure.

NUMERICAL RESULTS

Numerical evaluation of the developed flowfield model can verify its utility by assessing accuracy of predictions. In concert with examination of a practical jet-flap flow, a test program was conducted to verify factors affecting accuracy of the finite element algorithm, as embodied in COMOC, for turbulent flow predictions. Both the MLT and TKE closure models were evaluated, and a discussion of results is presented in the Appendix. The following studies were conducted using discretizations and closure model combinations so identified to yield accurate results.

Symmetry Plane Analysis of A Slot Nozzle-Jet Flap Flow

The basic geometry involves interaction of a high momentum flow with a free-stream, over and downstream of the terminus of a planar jet flap, see Figure 2. Many experimental configurations have employed rectangular slot nozzles to form the jet flow, with aspect ratios (slot width to height) in the vicinity of 50:1. Important three-dimensional effects are then limited to the extremum boundary regions while the core flow approximates a two-dimensional character. Experimental data were taken (ref. 38) on the symmetry center-plane downstream of a slot nozzle-jet flap configuration of aspect ratio 60:1. This case was selected to evaluate predicted distributions of mean flow velocity and turbulence correlation.

The basic experimental configuration and computational solution domains are illustrated in Figure 6. The jet flow is accelerated by the nozzle to a nominal $U_j = 120$ m/s. Due to the associated favorable pressure gradient, the \bar{u}_1 profile at the starting plane of the solution is nearly uniform. Immediately downstream of the nozzle, the jet flow interacts with the free-stream within the primary mixing region, and a turbulent boundary layer flow develops adjacent to the flap which erodes the inviscid potential core at a rate different from the free shear layer mixing in the primary region. The flap terminates at a sharp trailing edge. Immediately thereafter, a secondary mixing region is engendered between the jet boundary layer flow and the entrained flow. The initially zero \bar{u}_1 on the flap surface is rapidly accelerated within the immediate downstream vicinity of the flap terminus. The large x_2 gradient of \bar{u}_1 associated with the turbulent boundary layer is consequently dissipated, and acts in the process as a strong source term for generation of turbulence kinetic energy, see equation (44). Well downstream of the flap, the slot flow approaches a jet bounded by two free shear-layer mixing regions.

The computational simulation of this composite jet-flap flow was accomplished employing the 2DBL and 2DPNS solution options and the TKE closure model. The flowfield solution was initiated at the exit plane of the nozzle as noted in Figure 6. Since no experimental data were available to initialize the solution, a uniform profile for \bar{u}_1 at the nozzle was assumed, and \bar{u}_2 , k and ϵ were started at zero levels. (This corresponds to the slug-start discussed in the Appendix.) The lower portion of the nozzle flow was assumed to develop on the flap as a boundary layer completely isolated from the primary

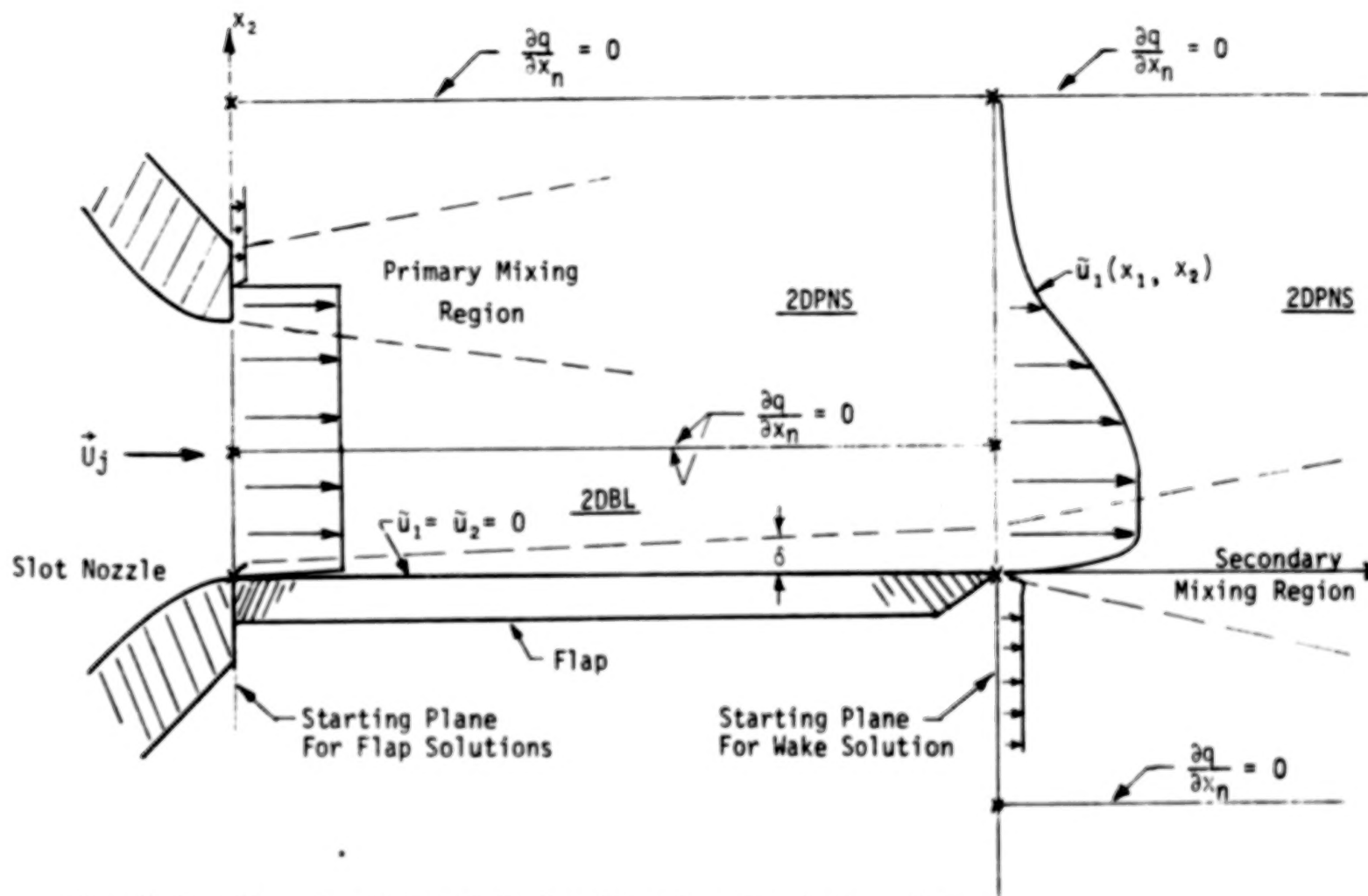


Fig. 6 Two-Dimensional Flowfield Specifications For Rectangular Slot Nozzle - Planar Jet Flap Configuration

mixing region shear flow by the jet potential core. This was considered adequate, since experiment verified that the gradient-free potential core persisted well into the wake, and the far-field pressure was the constant associated with a free-jet flow over a planar surface. The free-shear layer mixing within the primary region was initialized using a step-profile in \bar{u}_1 as noted in Figure 6, where the upper \bar{u}_1 entrainment velocity was estimated from experimental data profiles at $x_1/h = 6.6$, one-step height downstream of the flap terminus (ref. 38). These boundary layer and primary mixing region solutions were marched downstream and then matched together at the trailing edge, $x_1/h = 5.6$. A new solution domain was specified to encompass the two flows, plus the lower entrained flow, and a 2DPNS solution initialized to proceed into the wake region, see Figure 6. Again, the lower freestream \bar{u}_1 entrainment velocity was estimated from data, and was assumed laminar at the trailing edge. Boundary conditions for individual solutions within each domain are also noted in Figure 6.

Using the 2DBL option, the flap boundary layer flow was started from the assumed uniform nozzle profile by numerical solution of equation (52) for \bar{u}_1 assuming laminar flow and the no-slip boundary condition, $\bar{u}_1(x_1, 0) = 0$. Following the few integration steps required to establish derivatives, solution of equation (51) was initiated for computation of transverse velocity \bar{u}_2 , assuming a non-porous surface. Following a few steps to allow equilibration, the developing laminar boundary layer was tripped turbulent by signalling computation of effective viscosity, equation (50), using the MLT model, equation (55). The \bar{u}_1 and \bar{u}_2 profiles thereafter rapidly transform into the familiar turbulent profiles. The MLT solution was marched a short distance downstream, whereupon k and ϵ initial profiles were computed using the dual definitions for v_t equations (48) and (55). A restart of the entire solution was accomplished, and the turbulent boundary layer allowed to develop to the flap terminus using the TKE closure model, equations (53)-(54). The wall damping influence was retained within the TKE solution by over-riding the k and ϵ levels, computed from the differential equation solutions, by those computed from MLT at all nodes lying inside the transitional layer. Illustrated in Figure 7 is the development of the turbulent boundary layer profile in terms of the shape factor H . For a fully developed, laminar incompressible flat plate boundary layer, $H = 2.6$, while for a turbulent flow, $1.3 \leq H \leq 1.6$. The computed development spans the range.

The two-dimensional shear layer computation within the primary mixing region was similarly initiated from a slug start. However, the computed \bar{u}_1 profile at $x_1/h = 5.6$ exhibited a much larger potential core than did the experimental data of $x_1/h = 6.6$. This indicates that the associated turbulent mixing within the blunt base region at the nozzle face was grossly underestimated by the assumption of a thin shear layer. An accurate flow characterization in this region would require a complete Navier-Stokes solution, which could account for recirculation, as noted in the development. However, since the primary focus is on the secondary mixing region evolution, and since experiment shows the primary mixing region remains isolated downstream past $x_1/h = 6.6$, the free-shear layer solution was simply continued downstream a distance sufficient to erode the span of the potential core to essential agreement with the data. The numerical profiles for \bar{u}_1 , \bar{u}_2 , k and ϵ at one slot-height upstream of this location were then employed to initialize the combined wake solution.

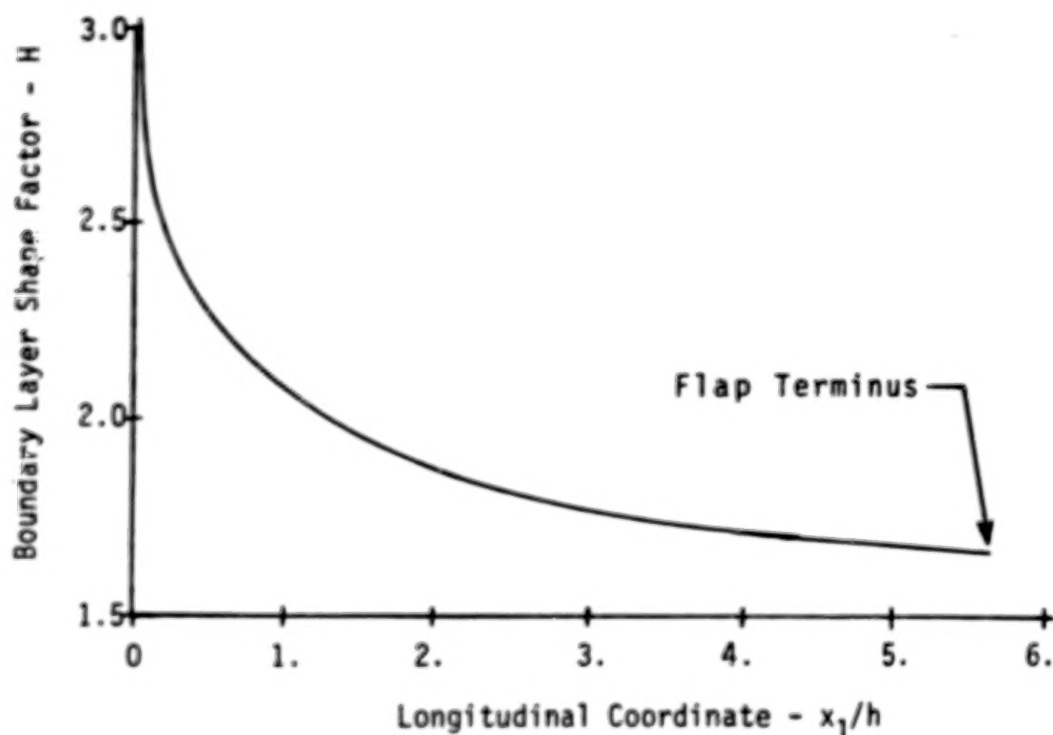


Fig. 7 Turbulent Boundary Layer Development Over Jet Flap

The developed two-dimensional boundary layer and shear layer solutions initialized the 2DPNS solution on the combined domain at the flap trailing edge. The boundary condition specifications are denoted in Figure 6. Shown in Figure 8 are computed distributions of \bar{u}_1 at select downstream stations, shown in comparison to experimental data at $x_1/h = 6.6$. Excellent agreement is illustrated, with the sole consequential difference at the wings of the \bar{u}_1 profile where the jet merges with the entrained flow. Shown in Fig. 9 are corresponding computed distributions of turbulent kinetic energy k , equation (13), in the primary and secondary mixing regions. Illustrated for comparison is the measured normalized x_1 component of the Reynolds stress, $-\bar{u}_1' u_1'$ (ref. 38, Fig. 24). Assuming isotropy, k and $\sqrt{\bar{u}_1' u_1'}$ would be directly comparable. Agreement is good within the secondary mixing region, wherein the initially small level at $x_1/h = 5.6$ has been consequentially increased by the terminus of the flap. Considerably poorer agreement is noted within the primary mixing region, a direct consequence of the less accurate starting conditions as discussed.

The illustrated agreement tends to confirm the validity of the wake flow initiation procedure as well as the appropriateness of the 2DPNS equation system. While the flow regions illustrated are important, the strong interaction zone immediately downstream of the flap terminus is of primary interest. The extremum mean flow gradients exist therein, both in the x_1 and x_2 coordinate directions, and the corresponding generation rate of turbulence is extremal. Shown in Figure 10 are axial mean velocity \bar{u}_1 profiles at various stations downstream of the trailing edge. Note that the initial zero level on the flap is rapidly accelerated to produce the typical shear layer profiles.

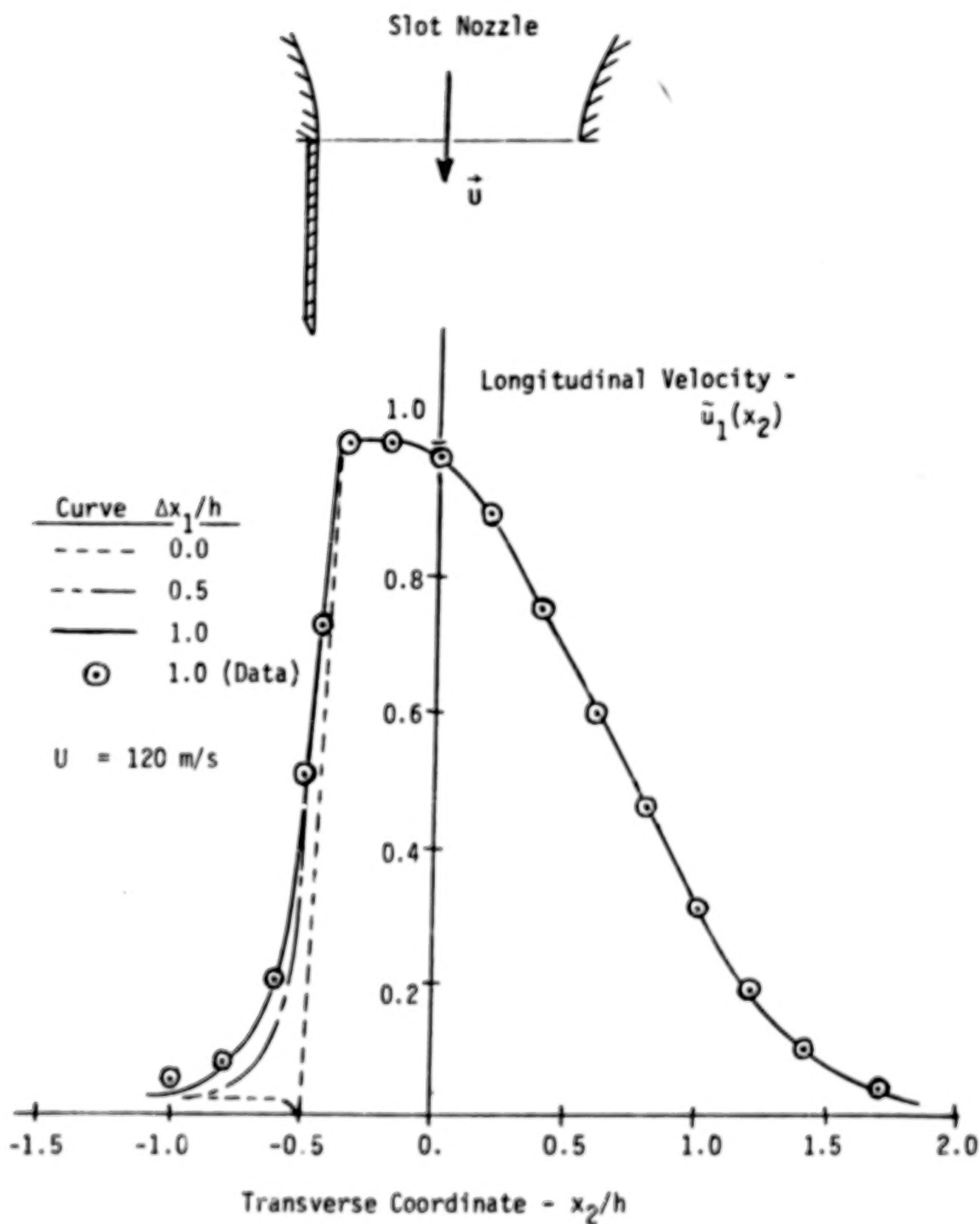


Fig. 8 Longitudinal Velocity Profiles Downstream of Jet Flap

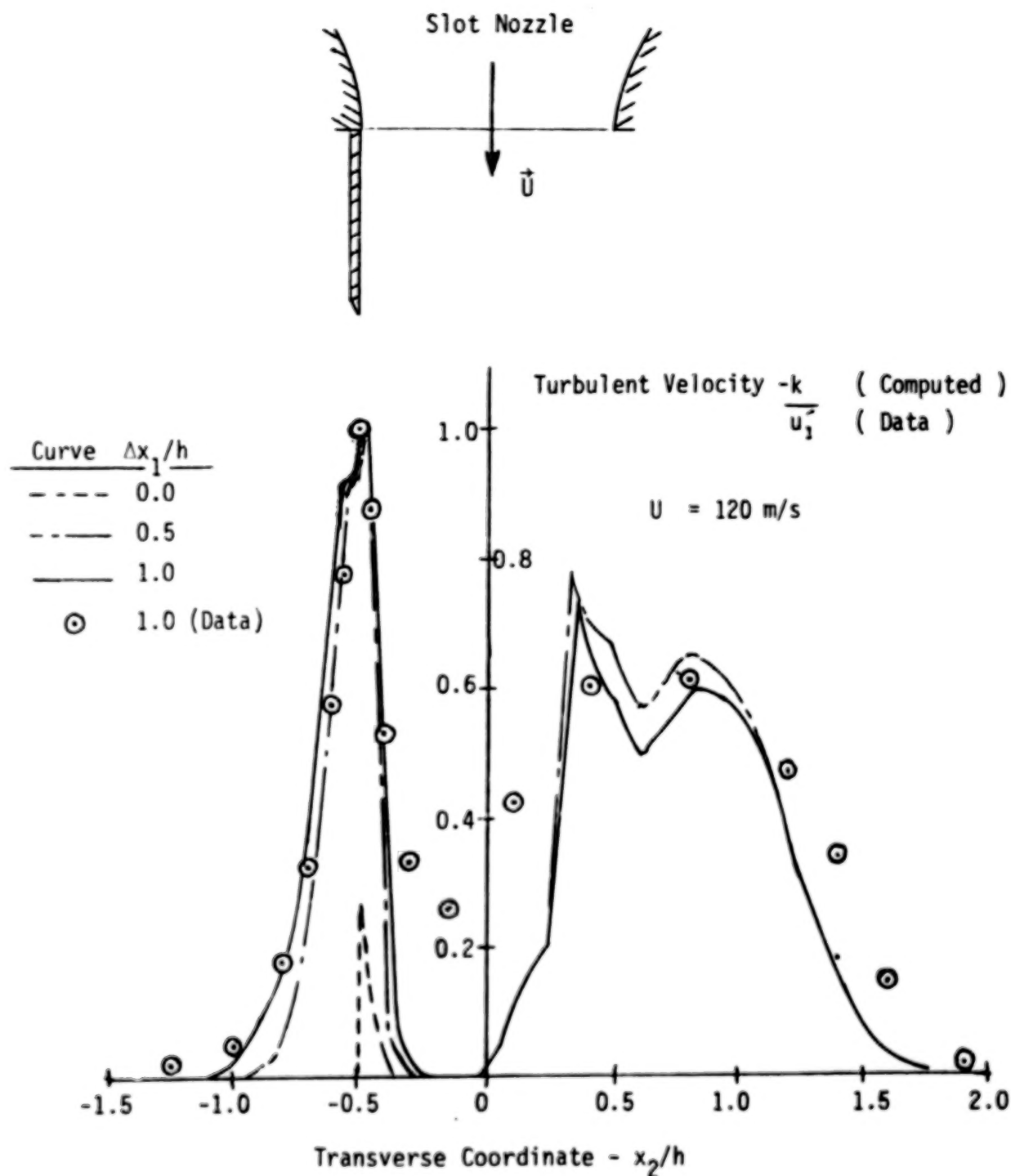
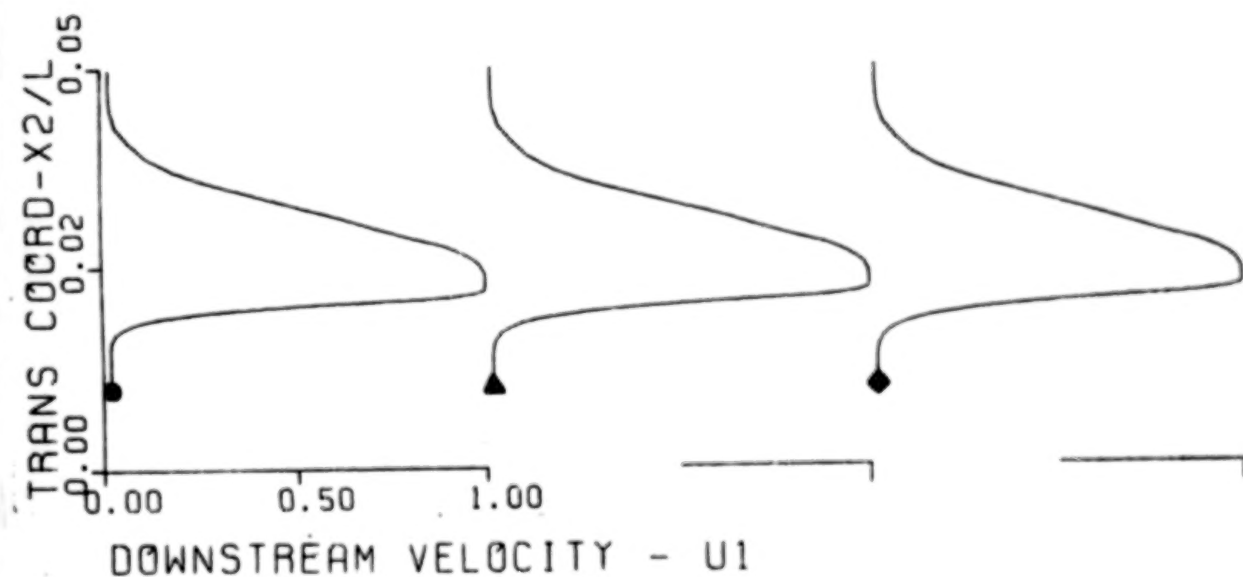
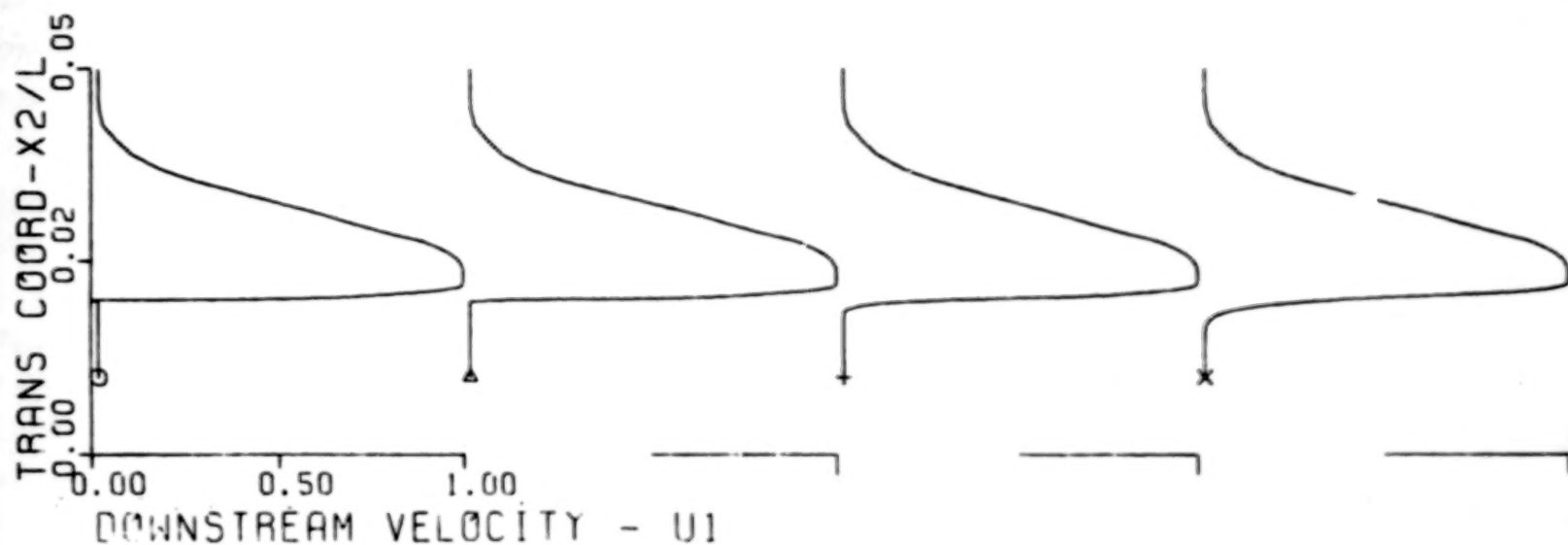


Fig. 9 Turbulent Velocity Profiles Downstream of Jet Flap



SYM	X_1/L
○	0.0560
△	0.0561
+	0.0570
×	0.0601
●	0.0622
▲	0.0642
◆	0.0660

Fig. 10 Mean Flow Velocity Profiles Downstream of Jet Flap Trailing Edge

Since a mean flow velocity gradient in the x_2 direction continually persists, turbulence kinetic energy k is correspondingly generated well downstream of the local x_1 acceleration at the trailing edge. Corresponding computed distributions of turbulence kinetic energy are presented in Figure 11 at identical stations downstream of the flap terminus. Following the initial maximum acceleration, the peak turbulence kinetic energy along a locus parallel to the flap in the wake continues to grow. The peak region broadens with distance downstream, and eventually generates a stepped peak. As a direct consequence, there results a pronounced overall increase in the level of turbulence within the flowfield due to the flap terminating.

Numerical evaluation of spatial derivatives of \tilde{u}_1 and k in the wake region could be employed in a noise model, for example, equation (16) augmented for the more general case. The peak x_1 derivative of \tilde{u}_1 immediately downstream of the flap terminus is of the order 10^7 , and decreases rapidly to 10^4 one slot height downstream. The \tilde{u}_1 derivatives in the x_2 direction, which contribute to the shear noise term, are also maximum at the trailing edge, rapidly decrease, and then continue to slowly decrease as the flow proceeds downstream. Calculated extremal values of $\partial\tilde{u}_1/\partial x_2$ in the immediate wake are the order 10^6 , decrease to 10^5 at one slot height and $.5 \times 10^5$ two slot heights downstream. The turbulent kinetic energy also contributes, and the extremal x_1 derivative of k is of order 10^7 . Lateral x_2 derivatives of k are also of order 10^7 , and persist well downstream of the trailing edge, as noted in Fig. 11. Recall that, as discussed, a noise model may utilize the eddy volume concept, the assumed-bounded region over which a non-zero correlation exists. A length scale for the eddy volume can be extracted from the computed turbulence parameters, see equation (47). Extremum dissipation lengths of .0075m and .0018m were calculated from the computed k and ϵ distributions. They compare favorably with .0082m and .0036m, as determined from experimental longitudinal and transverse space autocorrelation by Tam and Reddy (ref. 39).

Acoustically Modified Planar Jet-Flap

Treatment of an acoustically "hard" flap surface in the form of homogeneous or discrete surface porosity is experimentally verified to alter far-field acoustic intensity (cf., ref. 5, 10). An aerodynamically-acceptable procedure is to replace the hard flap with a mechanically-formed mesh surface, through which mass flow can be induced by generation of modest pressure differences. Attenuation of far-field sound power level may primarily result from alteration of the local turbulent flowfield, in particular the mean flow local shear stress distribution. Surface shear is basically $\partial\tilde{u}_1/\partial x_2$, which is the dominant source mechanism in unidirectional shear flows (see source terms in equations (53)-(54)). It is also a mean flow contribution to the "shear-noise" source term correlation for the Lighthill equation solution, for example equation (16). The local value of shear at the flap trailing edge can be expected to significantly affect the rate of momentum defect attenuation within the secondary mixing region, immediately downstream of the trailing edge, see Fig. 6. Therefore, in this instance of interest, surface treatment appears to induce acoustic modifications by alteration of the local detailed flowfield structure.

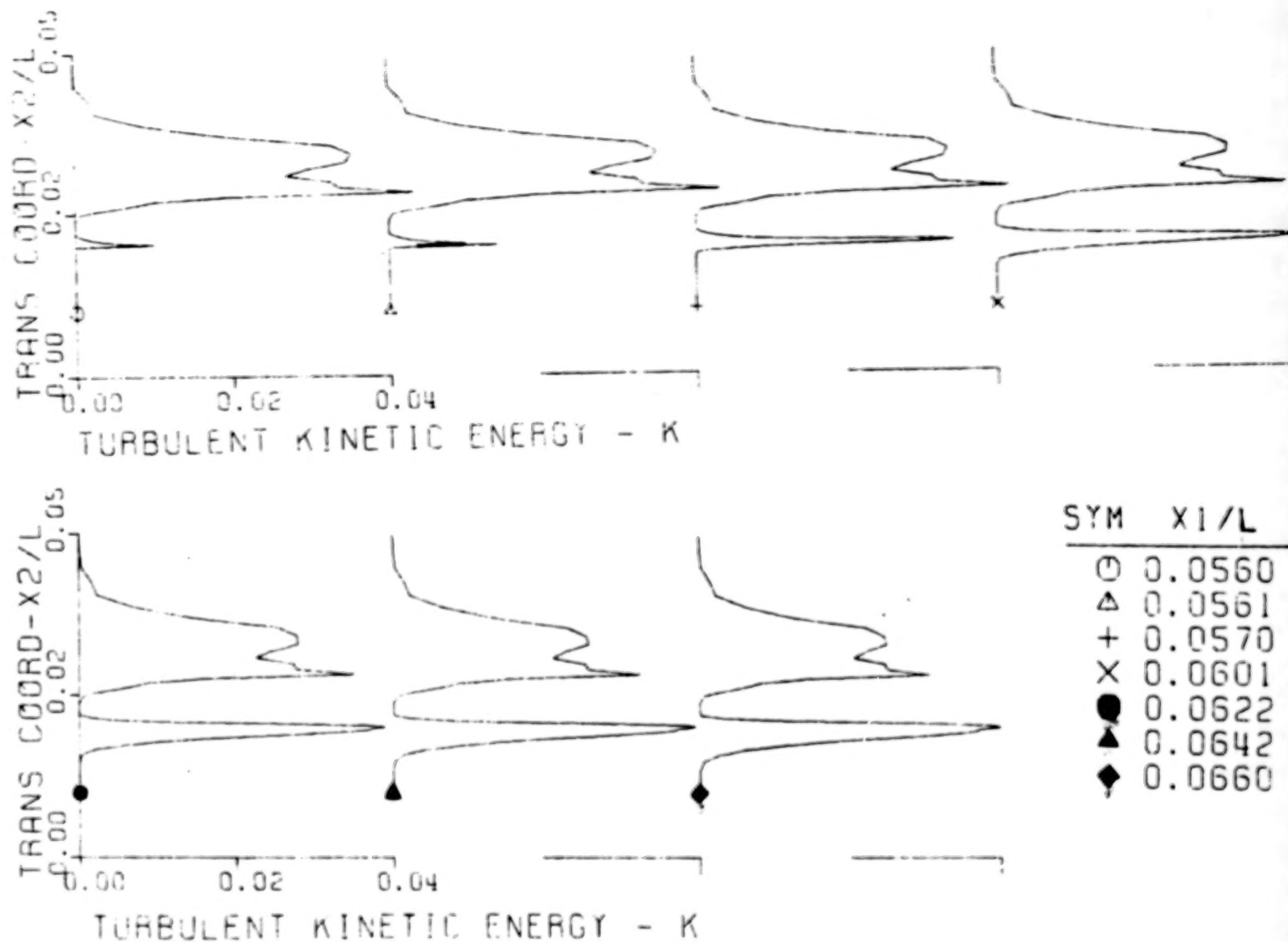
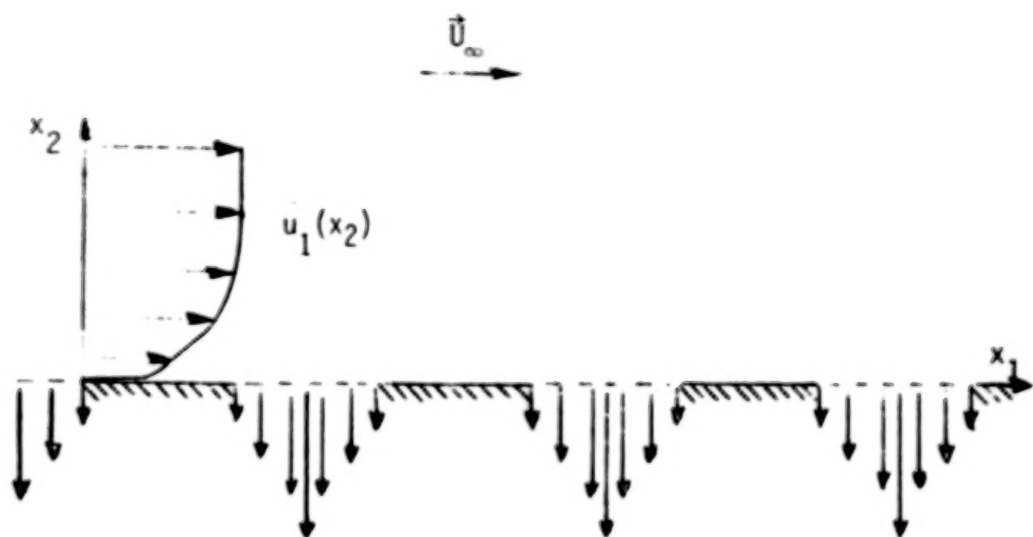
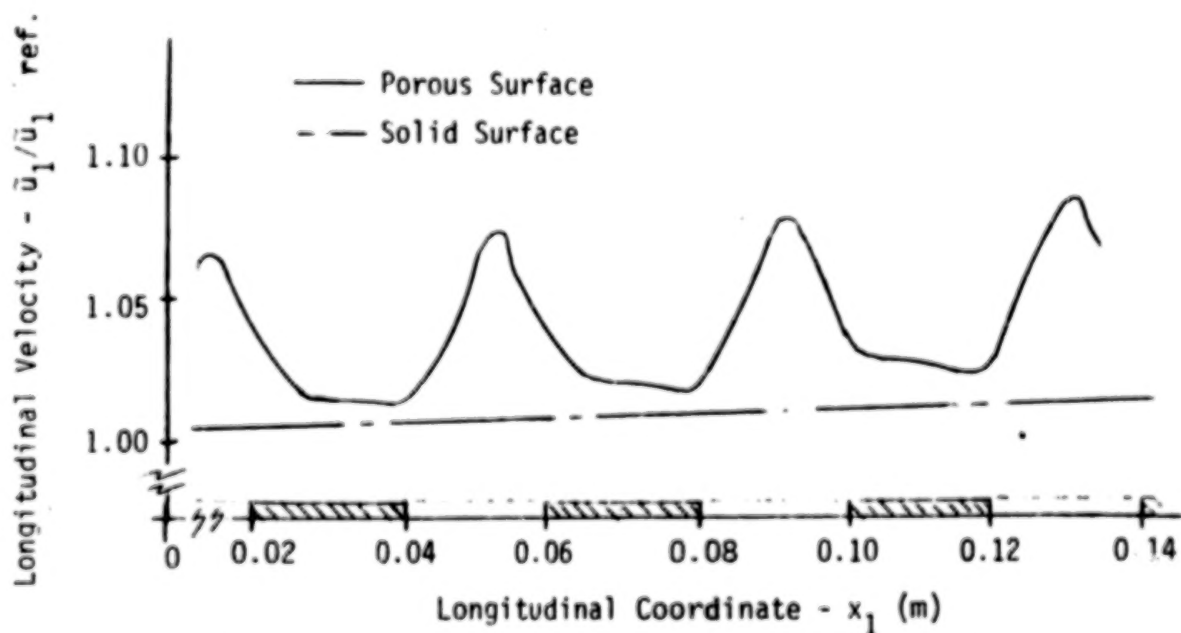


Fig. 11 Turbulent Kinetic Energy Profiles Downstream of Jet Flap Trailing Edge



a. Graph of Porous Surface Mass Flux Periodicity, $V_{\max} U_\infty^{-1} = .001$



b. Longitudinal Velocity Near Porous Surface - \bar{u}_1

Fig. 12 Influence of Porous Surface Treatment on Turbulent Flow

A computational simulation of the induced influence of surface porosity is particularly direct, since the equivalent boundary condition statement is a controlling mechanism of the numerical solution for the flowfield. While the actual mechanisms of pressure coupling may be rather complex, an elementary extension of the two-dimensional configuration was evaluated to examine the fundamental phenomenon. The acoustic surface treatment can be assumed correlated by an elementary form of Bernoulli's equation.

$$\Delta p = -c\rho_w V_w^2 \quad (76)$$

In equation (76), Δp is the pressure difference across the porous surface, $\rho_w V_w$ is the resultant induced colinear mass flux, and c is an experimental friction factor. The pressure difference exists between the exterior flow and a sub-surface cavity, which undoubtedly possesses a family of acoustic waves travelling at the characteristic cavity frequencies. Hence, one expects that Δp is a distributed function of x_1 ; dependent upon the cited factors, the induced V_w may be of variable sign and magnitude.

The concept was evaluated using the detailed velocity field for the Bradshaw relaxing flow test case as discussed in the Appendix. This standard case was altered by specification of a discrete and cyclic distribution of $\Delta p(x_1)$, equation (76), as graphed in Figure 12a. The induced normal mass flux velocity, V_w , acts directly as a boundary condition for solution of \tilde{u}_2 , equation (51), and indirectly as a modification to the turbulence wall damping function, equations (58)-(61). The flux period was approximately 0.02m, the wave-form a hat function with peak value $V_w/U_\infty = 0.001$ (i.e., mass flow into the cavity), and the x_1 span of surface treatment was approximately 0.15m. The flowfield variables were initialized from the standard case solution. Shown in Figure 12b is the computed x_1 distribution of \tilde{u}_1 , at the first finite element node above the flap surface (located at $x_2/\delta = 0.0013$, where δ is the local boundary layer thickness) in comparison to the standard case results. This modest efflux accelerates the local mean flow by up to about 10%, with a corresponding increase in $\partial \tilde{u}_1 / \partial x_2$. The period appears equal to the applied pressure wave, and the phase lags by about one-quarter of the period. The effective turbulent viscosity, equation (50), computed at this node increased by approximately 8% at peak V_w , which alters the corresponding value of k , equation (43), by about 15%. Reversal of the sign of Δp would induce deceleration of \tilde{u}_1 by about the same magnitude, and the levels of v^e and k would be correspondingly decreased. Elsewhere, away from the immediate vicinity of the surface, the computed \tilde{u}_1 profiles were unaffected by the wall phenomena for the periodicity and amplitude evaluated. These results indicate that a very modest transverse mass flux, as induced by a pressure difference across a porous aerodynamic surface, can significantly alter the local detailed structure of a turbulent boundary layer flow.

A corresponding influence on the local source mechanisms for acoustic phenomena could account in some part for measured alteration of farfield

intensity levels. In particular, the exact distribution of \bar{u}_1 and k at the flap terminus, as altered by transmission over the modified flap surface, could be important since this flow initializes the secondary mixing region. To assess influences, the discussed two-dimensional hard flap configuration of Schrecker and Maus (ref. 38) was computationally altered to induce a continuous distribution of surface porosity. The wave form approximated a sine with amplitude $V_w/U_\infty = \pm 0.03$ and period $\Delta x_1/h = 0.04$, where h is the slot nozzle height. In the downstream flap region, $5.0 \leq x_1/h \leq 5.6$, the standard case boundary layer flow was approaching fully turbulent with a shape factor $H = 1.6$, see Figure 7. This flow was rerun with the cited porosity distribution to determine the extremum induced modifications to H and the computed \bar{u}_1 directly above the flap surface. The results are summarized in Table 2.

TABLE 2

Porosity-Induced Jet-Flap Flowfield Modifications

Case		Velocity		Shape Factor H
No.	Description	Transverse V_w/U_j	Longitudinal \bar{u}_1/U_j	
1	Standard (Hard)	0	0.092	1.63
2	Influx (Soft)	+0.03	0.031	1.87
3	Efflux (Soft)	-0.03	0.148	1.57

The period of the flow alterations agreed with the specified influence and lagged in phase as discussed for the check case.

A 2DPNS solution in the trailing edge wake was completed to assess the influence of induced flowfield modifications upon evolution within the secondary mixing region. Solutions were initialized using mean flow velocity profiles for cases 2 and 3, that departed the furthest from the standard case 1. Table 3 summarizes the results in terms of longitudinal mean velocity and turbulence kinetic energy at two vertical (x_2) levels and at several downstream stations. Even though the porous efflux case 3 is initialized with larger \bar{u}_1 , both the standard and influx cases produce higher \bar{u} solution levels by $x_1/h = 0.32$. The standard case also produces extremal levels of k at this station, even though the initial levels for the efflux case 3 were five times larger. Note that by $x_1/h \approx 0.05$ for the standard case, computed levels for both \bar{u}_1 and k are approximately 80% of those predicted at $x_1/h = 0.32$. Hence, the initial turbulence mixing phenomena within the secondary mixing region occurs directly adjacent to the flap trailing edge, and appears quite sensitive to the detailed structure of the turbulent boundary layer flow at the flap terminus.

TABLE 3

Distribution of Mean Flow and Turbulence Velocities Within
Initial Secondary Mixing Region as Function of Simulated Flap Surface Porosity

Coordinates - x_i/h		Mean Flow Velocity - \bar{u}_i/U_j			Turbulence Kinetic Energy - k/U_j^2		
Downstream ($i = 1$)	Vertical ($i = 2$)	Influx Case 2	Standard Case 1	Efflux Case 3	Influx Case 2	Standard Case 1	Efflux Case 3
0.0	0.0014	.031	.094	.148	10^{-6}	10^{-6}	10^{-6}
	0.0	.0	.0	.0	.0	.0	.0
0.001	0.0014	.042	.081	.133	.0006	.0013	.0063
	0.0	.032	.050	.09	.0005	.0020	.0044
0.05	0.0014	-	.344	-	-	.0358	-
	0.0	-	.320	-	-	.0368	-
0.16	0.0014	.336	.378	.362	.0300	.0451	.0376
	0.0	.327	.370	.355	.0300	.0436	.0374
0.32	0.0014	.389	.414	.378	.0331	.0431	.0382
	0.0	.384	.408	.373	.0335	.0431	.0382

Recirculating Flow Within A Porous Slot

The discussed calculations confirm that transverse mass flux through a porous flap surface can produce significant changes in the detailed structure of the attached turbulent boundary layer flow. The influence of porosity was exerted only indirectly on the \bar{u}_1 solution through the wall damping function and the \bar{u}_2 boundary condition. Consequently, a computational evaluation was made of the direct influence within the immediate vicinity of a porous slot by numerical solution of the complete two-dimensional time-averaged Navier-Stokes system, equations (37), (38), and (65).

The test geometry corresponds to the flow over the first slot of the standard case as exhibited in Figure 12a. Both mass addition and deletion through the recessed base of the slot were evaluated. The solution domain geometry and boundary condition specifications are illustrated in Figure 13. Shown also is a representative discretization, illustrated with diagonals removed for clarity, consisting of 304 finite elements. The flow proceeds over the slot from the left, and upstream and downstream boundary conditions were established from the boundary layer solution using equations (35)-(36). Along the top of the domain, the gradient boundary condition on streamfunction allows the flow to respond to the cavity presence, i.e., the closure segment is not forced to be a streamline. Along the cavity base, V_w was assumed a linear function of x_1 with a maximum efflux/influx of $V_w U_\infty^{-1} = \pm 0.015$.

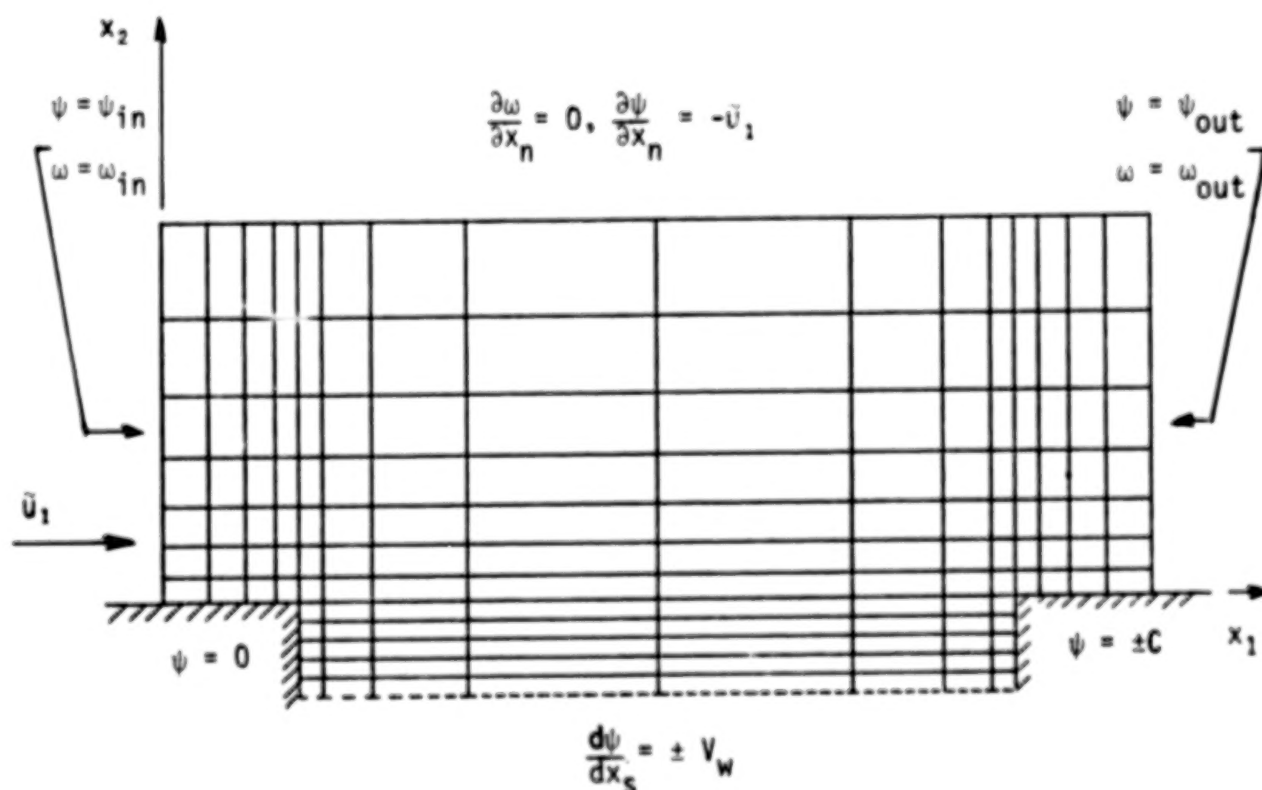


Fig. 13. Finite Element Discretization And Boundary Conditions For Slot Region Recirculating Flow Analysis

The depth of the slot was approximately 0.5% of δ the local boundary layer thickness. The flow Reynolds number based on δ and U_∞ is 10^5 . The slot Reynolds number based on shear velocity, equation (62), and slot depth, was 24, indicating that the contained flow was fully dominated by wall damping. Hence, the effective viscosity μ^e for all nodes within the slot was assumed laminar. MLT was employed to compute v_t , equations (55)-(64), at all nodes above the original plate surface, as in the standard non-porous surface case. The top node row of the solution domain lies within the fully turbulent flow.

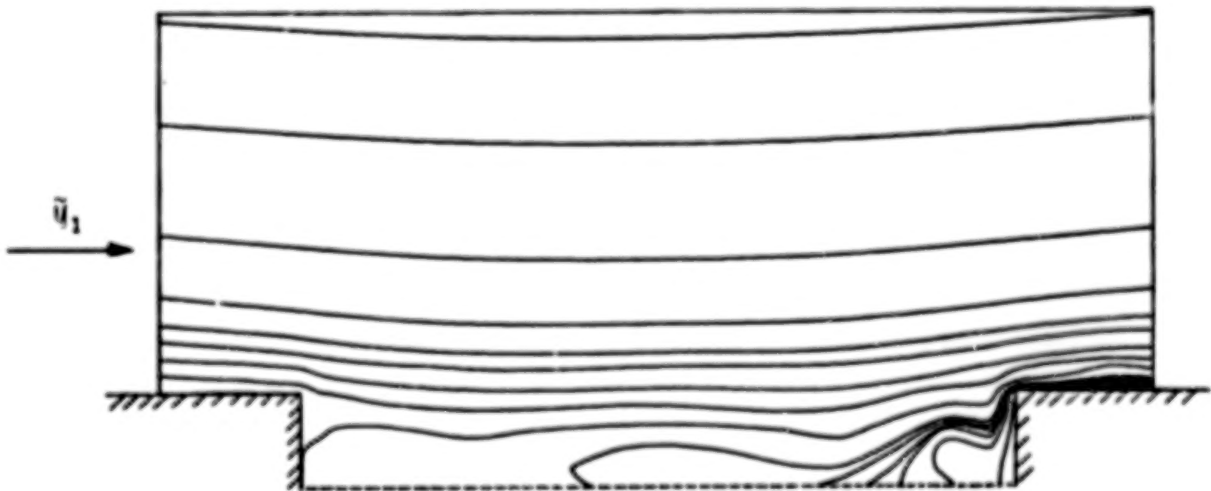
Computed steady flow streamline distributions are shown in Figure 14a,b, for mass removal and mass addition through the slot base, respectively. For both cases, the far-field streamlines are computed concave downward indicating the effect of presence of the slot permeates the entire domain. Somewhat less concavity occurs for mass addition since identical farfield streamline levels are plotted for each case. The detailed flow structure in the immediate vicinity of the slot depends strongly on the sign of V_w . For mass removal, Figure 14a, the boundary flow generally overshoots the slot and circles back along the base, establishing a closed circulation contour at the downstream extremity. Mass addition, Figure 14b, appears constrained to the slot region with emergence into the main boundary flow occurring at the downstream step face. Hence, within the assumptive constraints and for the specified boundary conditions, the more complete Navier-Stokes solutions further illustrate the character of flowfield alteration induced by a porous surface. These results are at best indicative however, since the flow through the cavity base was specified a priori, rather than being coupled to resonance phenomena within a sub-surface cavity. Nevertheless, they do confirm the potential capability to numerically establish detailed flowfield data of impact in an aeroacoustic analysis.

An Elementary Three-Dimensional Evaluation

The discussed numerical evaluations are constrained to flows on the symmetry plane of a three-dimensional flowfield. The three-dimensional flows associated with practical OTW configurations on airfoil surfaces, cf., Figure 1, are considerably more complex than amenable to analysis using the employed equation systems. However, for a rectangular slot-nozzle-planar jet flap geometry with quiescent freestream, such as that of ref. 38, an exploratory evaluation of the potential of a three-dimensional solution can be established. Remaining within the boundary layer order of magnitude analysis, equation (34), and for the uniform freestream pressure field associated with rectilinear flow over a non-lifting surface, the mean flow between the jet symmetry plane and a lateral freestream, see Figure 2, can be approximated to first order as predominantly boundary layer with negligible lateral velocity (\bar{u}_1). Correspondingly, transverse mean velocity \bar{u}_2 can be initially determined over the flap from the continuity equation solution equation (51), and thereafter by solution of the three-dimensional \bar{u}_2 momentum equation, i.e., $i = 2$ in equation (52) and using equation (50).



a. Steady Flow Mass Removal Through Cavity Base



b. Steady Flow Mass Addition Through Cavity Base

Fig. 14. Computed Steady Flow Streamline Distributions For Turbulent Flow Over A Jet-Flap Slot.

A finite element discretization (less diagonals) of the left-half solution domain for the three-dimensional jet flap of Figure 2 is shown in Figure 15. Approximately 480 triangular elements are employed with non-uniformity specified to resolve the wall layer immediately adjacent to the upper and lower flap surfaces. The boundary condition constraints for the example solution are noted as well. As the flow departs the sharp trailing edge, the indicated wall boundary conditions are removed, as discussed for the two-dimensional solutions. A variant of the slug start was employed to initialize the solution field by interpolating the computed symmetry plane velocity distribution for \bar{u}_1 to a zero level at the lateral freestream. Following initialization and equilibration of the computed \bar{u}_2 profiles, closure for turbulence was switched from MLT to TKE, and the solution marched downstream to a distance sufficient to smooth the solution field. The trailing edge was assumed to exist at this point and the solution restarted with the flap (i.e., boundary conditions) removed to simulate emergence into the wake.

Shown in Fig. 16 is a surface representation of the computed equilibrated \bar{u}_1 distribution at the flap trailing edge. The grid imposed on the solution surface is identical to the employed discretization which serves to document appropriate refinement. The \bar{u}_1 velocity beneath the flap is assumed zero, and the additional grid detail therein has been omitted for clarity. The computed distribution of k at the trailing edge is shown in Fig. 17a. The centroidal spine is a consequence of the lateral derivatives of \bar{u}_1 , i.e., $\partial u_1 / \partial x_1$, as produced by the appropriate contour in Fig. 16 which serves as a source contribution for turbulence kinetic energy, see equation (53). The peak directly above the flap is the three-dimensional equivalent of the results illustrated in Fig. 9. The extent and location of the flap is noted, and the lower discretization detail is again omitted. Fig. 17b illustrates the computed k distribution at $\Delta x_1 / h = 0.02$ downstream of the flap terminus, as well as the lower discretization. The surface shape is unaltered everywhere except at the elevation of the flap terminus where a sharply spiked double peak has replaced the single peak illustrated in Fig. 17a. Hence, the existence of the trailing edge has resulted in rapid production of turbulence kinetic energy in agreement with the results of the symmetry plane evaluation. These three-dimensional predictions, while the result of a highly simplified analysis for an elementary geometry, do confirm the potential to extend the developed flowfield model to the three-dimensional configurations of practical interest.

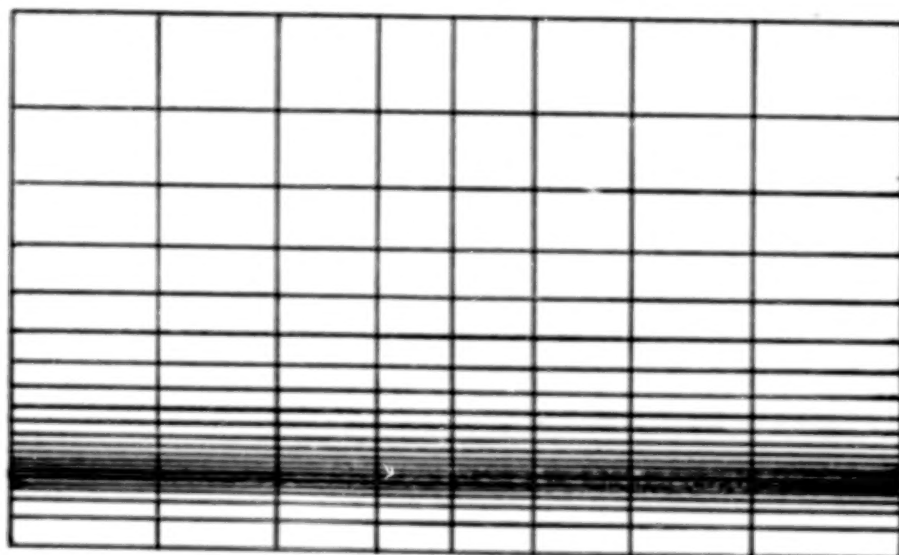


Fig. 15. Finite Element Discretization For Three-Dimensional Solution

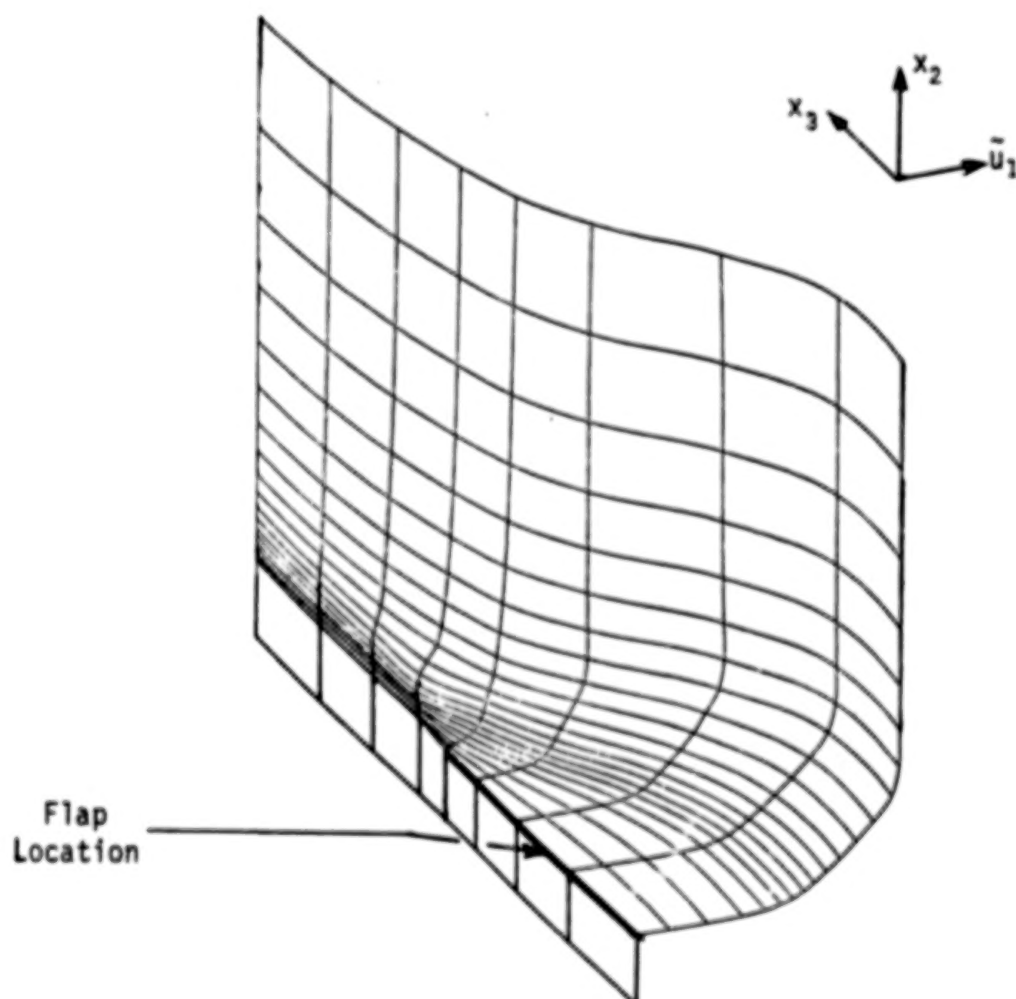


Fig. 16. Computed \bar{u}_1 Distribution At Flap Trailing Edge

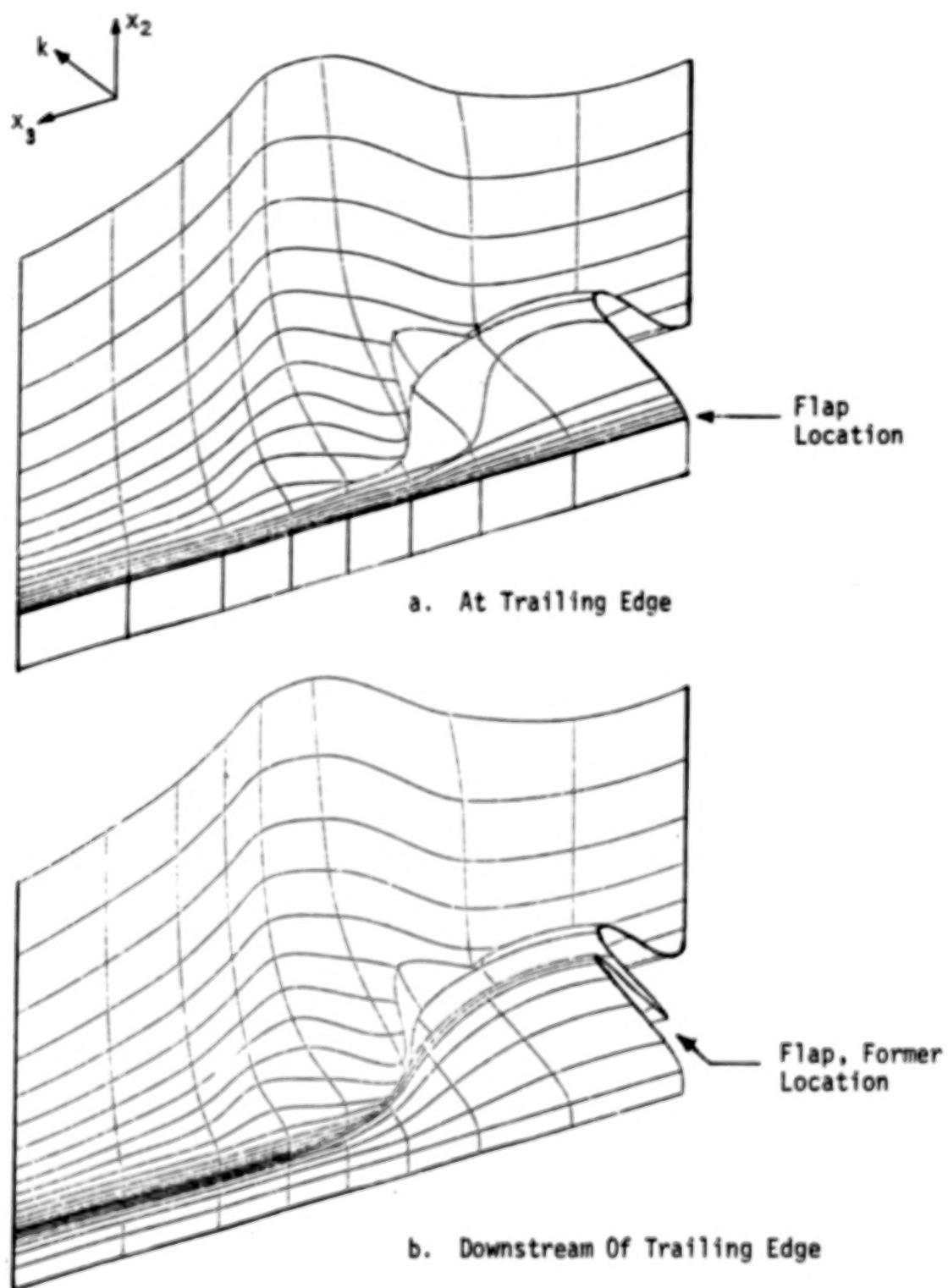


Fig. 17. Computed Turbulence Kinetic Energy Distributions

CONCLUDING REMARKS

Simplified forms of the Navier-Stokes equations for describing aero-acoustic flows over a basic jet-blown flap configuration have been established. A finite element formalism is employed to cast the identified initial-boundary value equation systems for steady, time-averaged turbulent flows into equivalent larger order systems of ordinary differential and/or algebraic equations. Numerical solutions were established using the COMOC computer program. Computed evolution of the turbulent flow on the symmetry centerplane of a rectangular slot-nozzle-planar jet flap geometry, and downstream of the sharp-edged terminus of the flap, compared favorably with experimental data. The influence of a porous treatment of the flap surface on the detailed flow structure on and downstream of the flap terminus, was evaluated using two equation systems. An elementary extension to a three-dimensional flow configuration was evaluated.

These results generally confirm the validity of the suggested approach to characterization of the turbulent aeroacoustic flows associated with directed-jet lift augmentation systems. In particular, use of the parabolized approximation to the full Navier-Stokes system appears appropriate for turbulent flows departing a sharp trailing edge of a planar flap. Extension to a curved flap surface requires development of a more comprehensive equation system, capable of computing pressure distributions in the plane transverse to the direction of predominant flow. This system should also be capable of predicting the entrainment induced by these lateral pressure gradients. Analysis of aeroacoustic flows over flaps with a blunt trailing edge using the parabolized equation systems is inappropriate in regions with flow separation and recirculation. The present results indicate that the more complete analysis can be locally imbedded within a parabolic solution. In this instance, additional attention is required to adequately accomplish closure for turbulence phenomena in flow regions with small turbulence Reynolds number. Extension to these areas should render the developed concepts directly applicable to aeroacoustic flowfield determination for practical lifting configurations.

APPENDIX

Initiation and Accuracy of Turbulent Flow Prediction

A computational test program was completed to assess factors affecting solution accuracy of turbulent boundary layer flows predicted using the finite element solution algorithm. The standard two-dimensional boundary layer equations (2DBL) are a sub-set of equations (51)-(54), with equation (52) for $j = 2$ discarded and $\ell = 2$ only, elsewhere. Equations (53)-(54) are solved for the turbulent kinetic energy (TKE) closure, using equation (50) to evaluate effective viscosity. For mixing length theory (MLT), the turbulence kinematic viscosity in equation (50) is determined algebraically using equation (55).

The three evaluations required to attest to solution accuracy relate to verification of mathematical order-of-accuracy, turbulent flow solution initiation from an assumed mean-flow velocity profile, and the hybrid closure model employing MLT concepts within the wall layer to provide boundary conditions for the TKE solution. Regarding the first item, confirmation of a formal order-of-accuracy is currently evaluable only for laminar flows. The selected test case is laminar, incompressible flow at zero external pressure gradient, the well known Blasius similarity solution (ref. 35). The fundamental error norm for a finite element solution is the energy norm (cf., ref. 40), defined for the linear equivalent of equation (66)-(67) as

$$E(q, q) \equiv \frac{1}{2} \left[K \int_R \frac{\partial q}{\partial x_\ell} \frac{\partial q}{\partial x_\ell} d\tau - \lambda \int_{\partial R} a^{(1)} q^2 d\tau \right] \quad (A.1)$$

The 2DBL system is not linear, but the non-linearity exists in the lower-order convection terms only for laminar flow which would not constitute a quadratic contribution to equation (A.1). Assuming the validity of equation (A.1) for the 2DBL system, and for use of simplex finite element functionals, equation (71), convergence of the numerical solution is theoretically (ref. 40),

$$E(q - q_m^*, q - q_m^*) \leq C L_m^2 \max |\tilde{u}_1''|^2 \quad (A.2)$$

where C is a constant independent of L_m , the measure of the smallest finite element spanning R , and \tilde{u}_1'' is the second x_2 derivative of \tilde{u}_1 and assumed continuous on R . Hence, under discretization refinement, convergence should be quadratic in the energy norm. Since the Galerkin criteria for the finite element algorithm, equation (73), renders the error orthogonal to the approximation base, the exponent of two in equation (A.2) can be numerically confirmed by measuring the finite element solution energy, equation (A.1)

$$E(q^*, q^*) = \frac{1}{2} \sum_{m=1}^M \left[\int_{R_m} K \frac{\partial q_m^*}{\partial x_\ell} \frac{\partial q_m^*}{\partial x_\ell} d\tau - \lambda \int_{\partial R_m \cap \partial R} a^{(1)} q_m^{*2} d\tau \right] \quad (A.3)$$

under discretization refinement. In equation (A.3), q_m^* is the finite element approximation functional, equation (71), ultimately evaluated in terms of the computed nodal distribution of the mean longitudinal velocity $\bar{u}_1(x_1, x_2)$. Shown in Fig. A.1 is the computed finite element solution energy, equation (A.3), evaluated at a specific x_1 station for $10 \leq M \leq 80$, where M is the nominal number of finite elements spanning $R(x_1)$. The slope is almost identically two, indicating that the expected convergence rate is achieved by the computational embodiment of the algorithm.

The laminar flow results were obtained using a uniform finite element discretization. However, a mandatory key feature for turbulent flow computations is use of highly non-uniform discretizations to obtain satisfactory computational efficiency in concert with acceptable solution accuracy. Following numerical tests, solution speed and accuracy were both enhanced using a finite element discretization, variable according to a geometric progression as

$$\eta_{m+1} = \eta_1 + s \sum_{j=2}^{m+1} \rho^{j-2} \quad 1 \leq m \leq M \quad (\text{A.4})$$

In equation (A.4), η_{m+1} is the extremum nodal coordinate of R_m and η_1 is the coordinate of the first node of the discretization, typically zero. Furthermore, ρ is the progression ratio and s is a scale factor that allows imbedding a given number of finite elements on R . Shown in Fig. A.2 are graphs of discretizations using equation (A.4) for several s/δ and ρ . Curves A, C and D illustrate uniform discretizations; the header shows the corresponding number of finite elements M spanning δ and 3δ , where free-stream boundary conditions are applied. Curve B illustrates a modestly non-uniform grid, suitable for laminar flow predictions. Curve E is the finite element discretization determined by numerical experiment to yield good solution accuracy for turbulent flow predictions in concert with minimal computer time. The finite element at the wall spans $\delta \times 10^{-3}$, yielding excellent resolution, yet only 28 finite elements are needed to span $R = 3\delta$.

Basic solution accuracy for a 2DBL turbulent flow was evaluated by comparison of a zero pressure gradient, flat plate computation to the experimental data of Wieghardt (cf., ref. 36, Vol. II, IDENT 1400). Solution initiation was accomplished assuming existence of a uniform \bar{u}_1 profile at the plate leading edge and the MLT closure model. Boundary conditions at the plate surface are $\bar{u}_1 = \bar{u}_2 = 0$; at freestream, $x/\delta = 3$, the vanishing gradient was imposed, $\partial \bar{u}_1 / \partial x_2 = 0$. The initial distribution for u_2 was zero since $\partial \bar{u}_1 / \partial x_1 = 0$ upstream of the plate. This specification corresponds to a "slug-start," the method employed to initiate solutions in the absence of any preferable alternative. Since the turbulent Reynolds number of the Wieghardt case is initially small, transition from laminar to turbulent flow occurs over a finite span of x_1 . The results of computational experimentation with the switch from laminar to turbulent flow is shown in Fig. A.3, in terms of skin friction obtained from wall shear by non-dimensionalization with $\frac{1}{2} \rho_\infty U_\infty^2$, see equation (63). The comparison experimental results were obtained from data using interpolation and the Ludwig-Tillman formula, equation (64). In each case, the flow was computed laminar to the selected transition point,

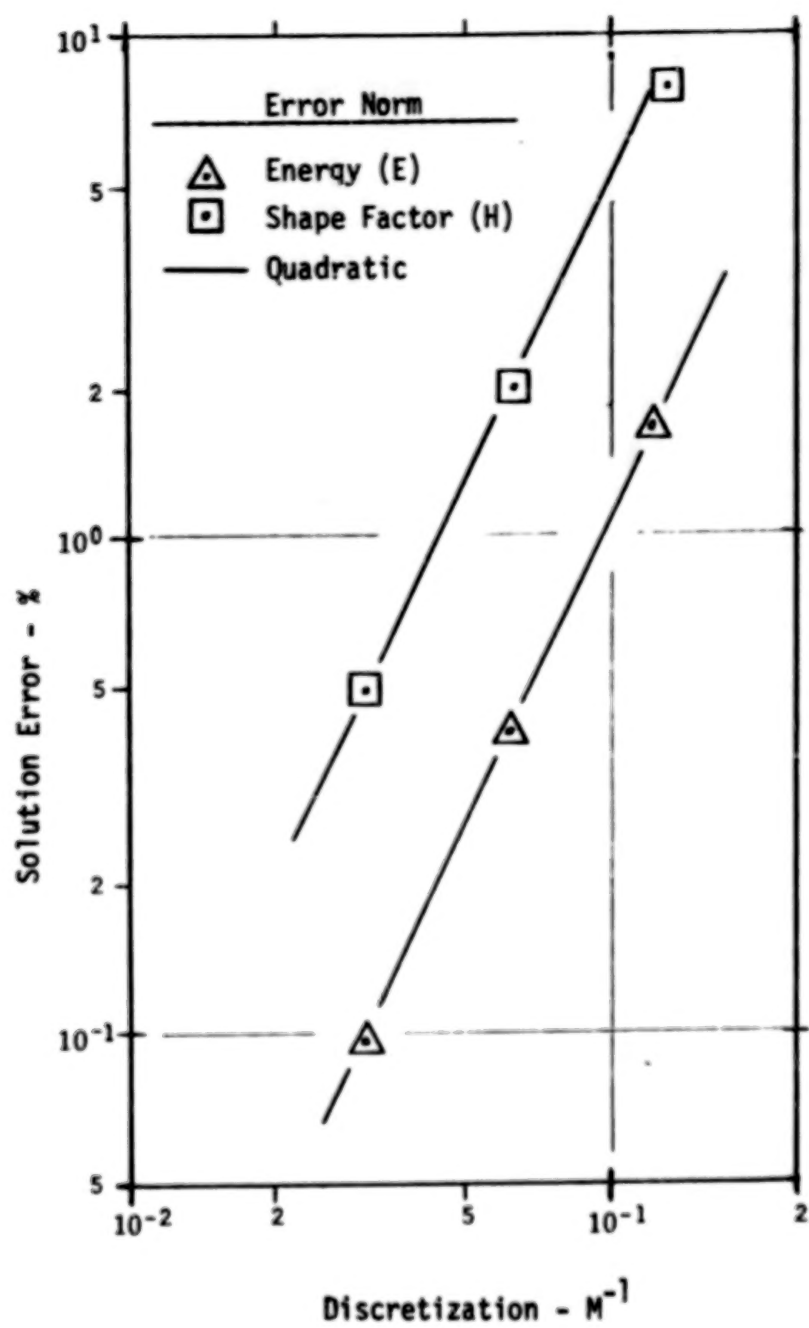
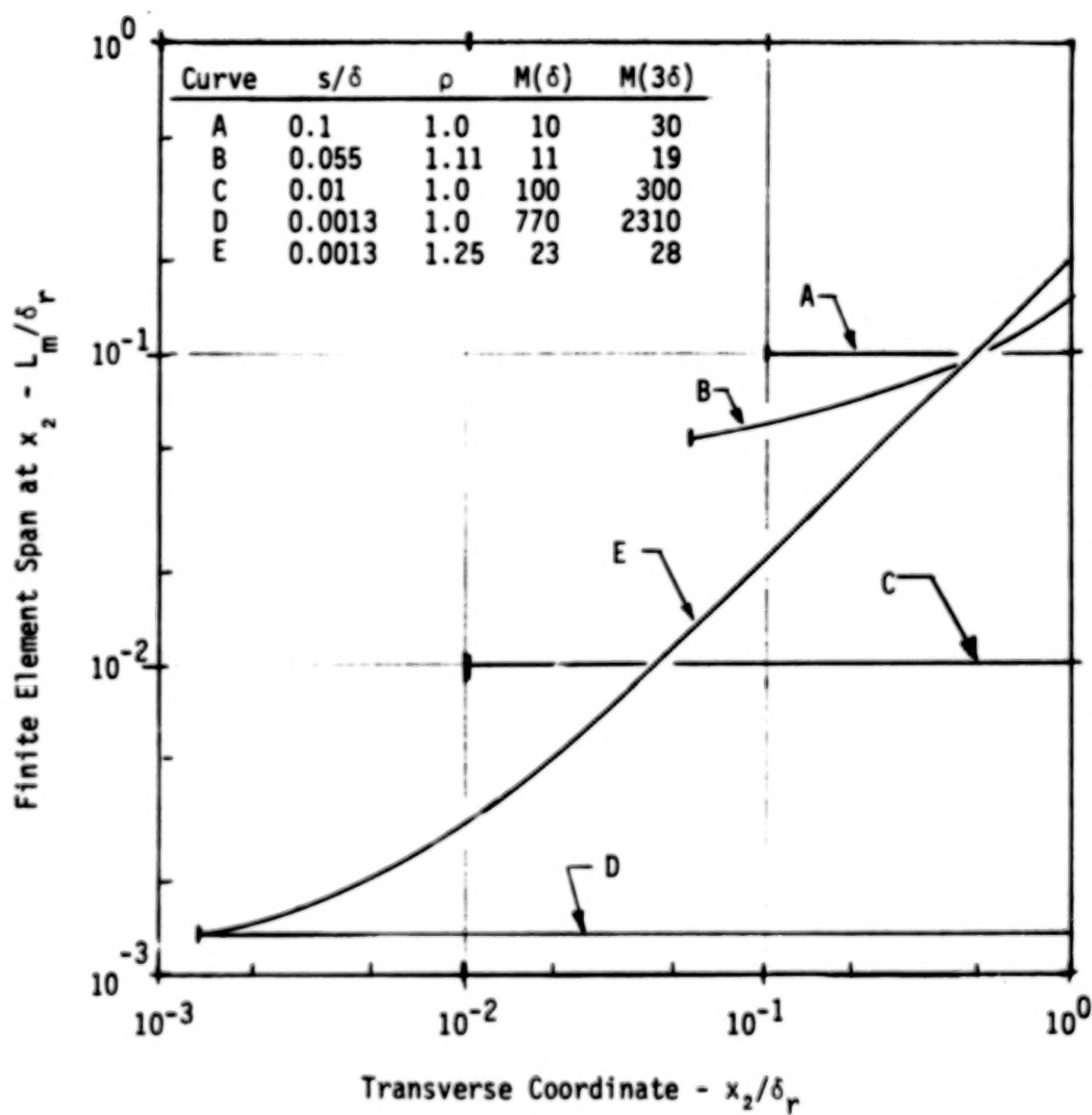


Fig. A.1 Finite Element Solution Convergence



WIEGHARDT FLAT PLATE FLOW (IDENT 1400)

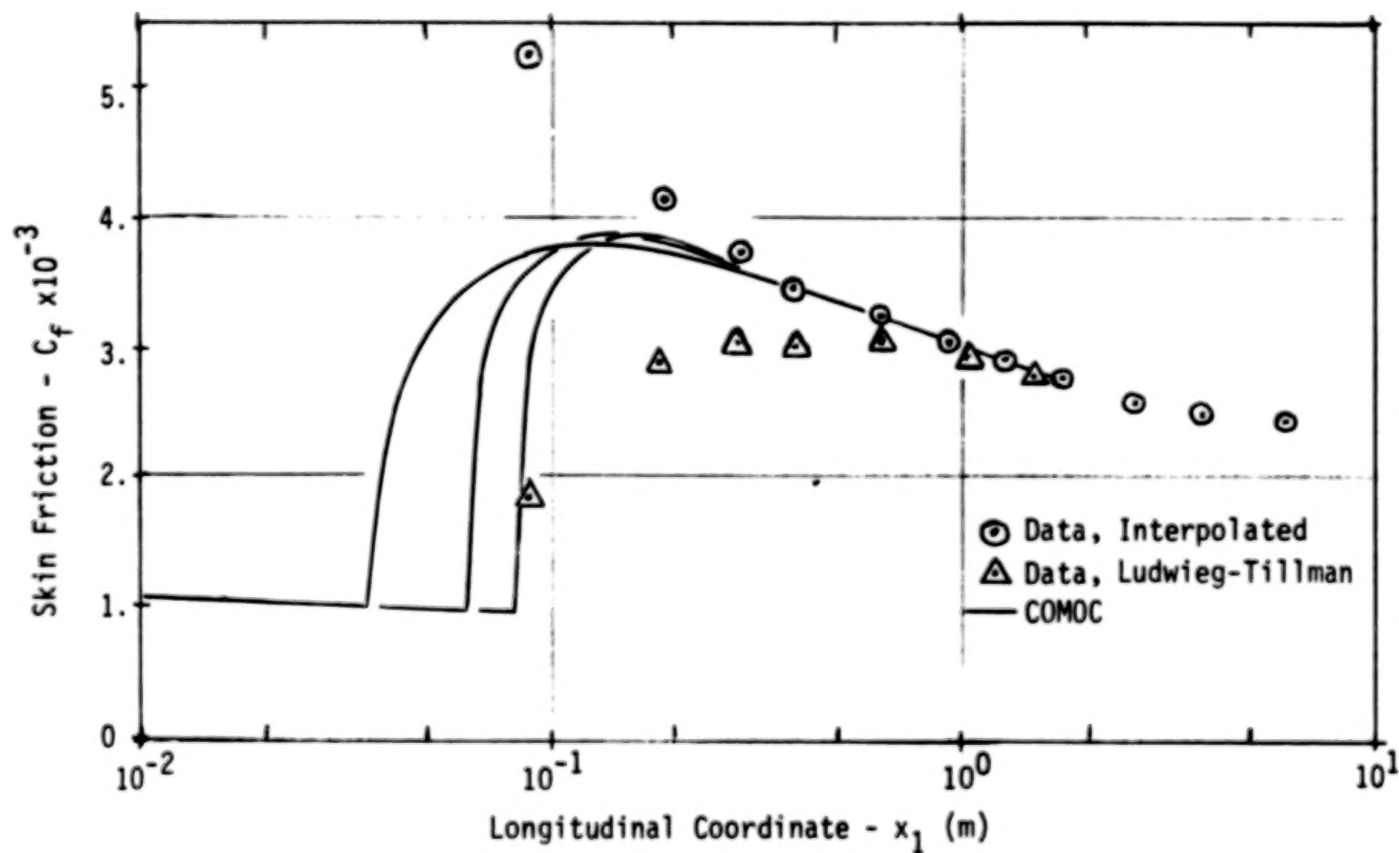


Fig. A.3 Transition Location Influence on Skin Friction, Wieghardt Flat Plate Flow, MLT

and no transition model was employed to alter the intermediate profiles. The family of computed results are bracketed by the data, and by $x_1 = 0.6m$ the various methods are in essential agreement. Corresponding comparison of computed \bar{u}_1 velocity profiles to data indicate excellent agreement, see Fig. A.4. These results confirm the slug start solution initiation procedure for the selected planar jet-flap evaluations.

The third requirement, to attest solution accuracy using the hybrid TKE-MLT closure model, was evaluated using as a comparison basis the experimental data of Bradshaw (ref. 36, Vol. II, IDENT 2400). Shown in Fig. A.5 are computed \bar{u}_1 velocity profile distributions, illustrating the agreement with data attainable using the MLT closure model. Overall, the comparison is quite good, although diffusional processes within the flat mid-range appear high as evidenced by the computed results uniformly exceeding the data. These differences diminish further downstream, but there is a corresponding trend to underpredict the first knee in the curve. Shown in Fig. A.6 is the same comparison to data with results computed using the TKE closure model. In the wall dominated viscous sub-layer, MLT was employed to compute near-wall boundary values of k and ϵ , for numerical solution of equations (53)-(54). As previously mentioned, the MLT evaluation also yields the initial distributions for k and ϵ . A vanishing normal gradient for k and ϵ was enforced at the freestream, and computed agreement with data is comparable to the complete MLT run. Detailed differences do exist however, as illustrated in Fig. A.7, on the multiple comparison bases of boundary layer integral parameters. The TKE solution does tend to overpredict both displacement and momentum thickness in comparison to the MLT solution. Otherwise the results are quite comparable and confirm the basic concept of the hybrid closure model for initiation of a parabolic solution in the wake downstream of a sharp trailing edge.

WIEGHARDT FLAT PLATE FLOW (IDENT 1400)

Station(m)

COMOC:

Data: 0.087 0.187 0.287 0.387 0.487 0.637 0.937 1.237 1.687

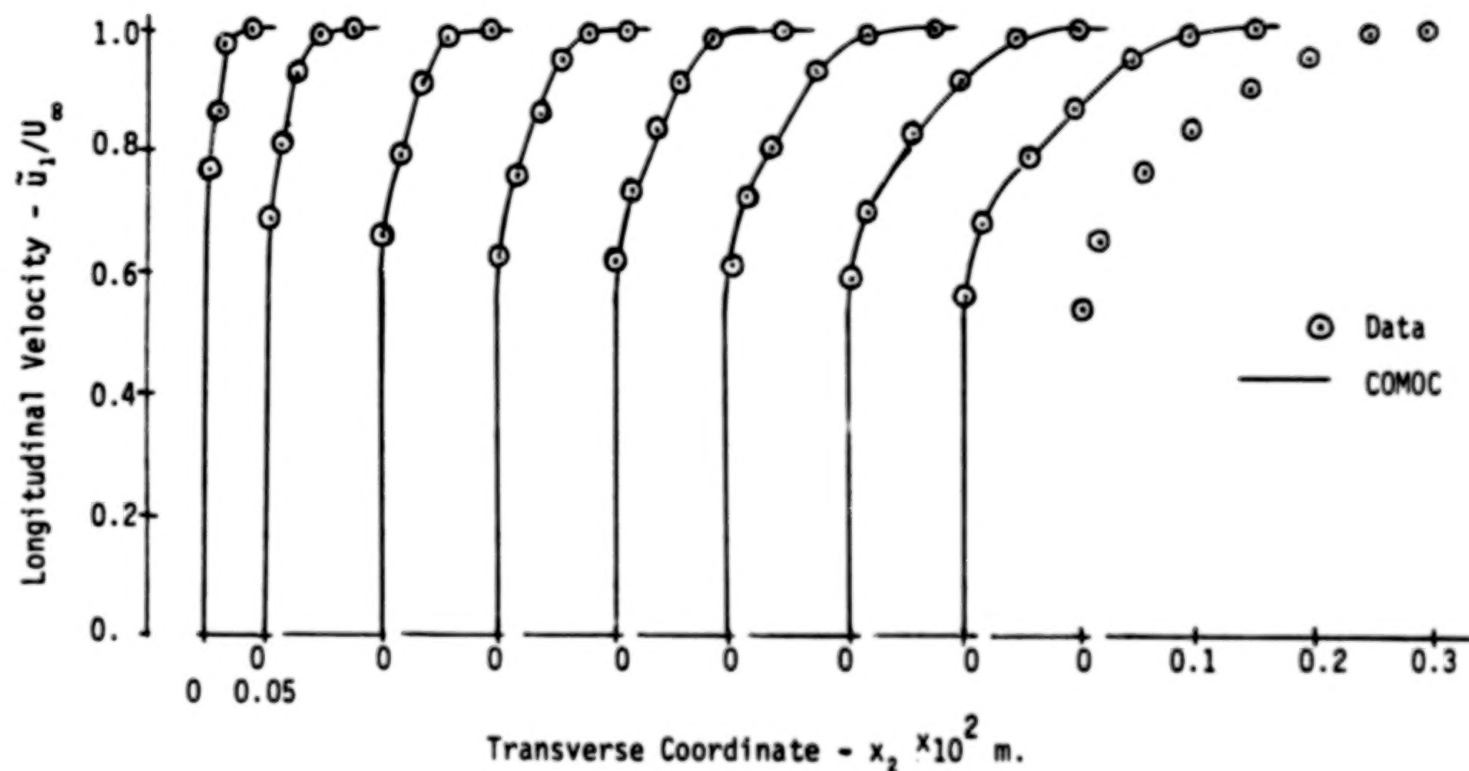


Fig. A.4 Longitudinal Velocity Profiles, Wieghardt Flat Plate Flow, MLT.

BRADSHAW RELAXING FLOW (IDENT 2400)

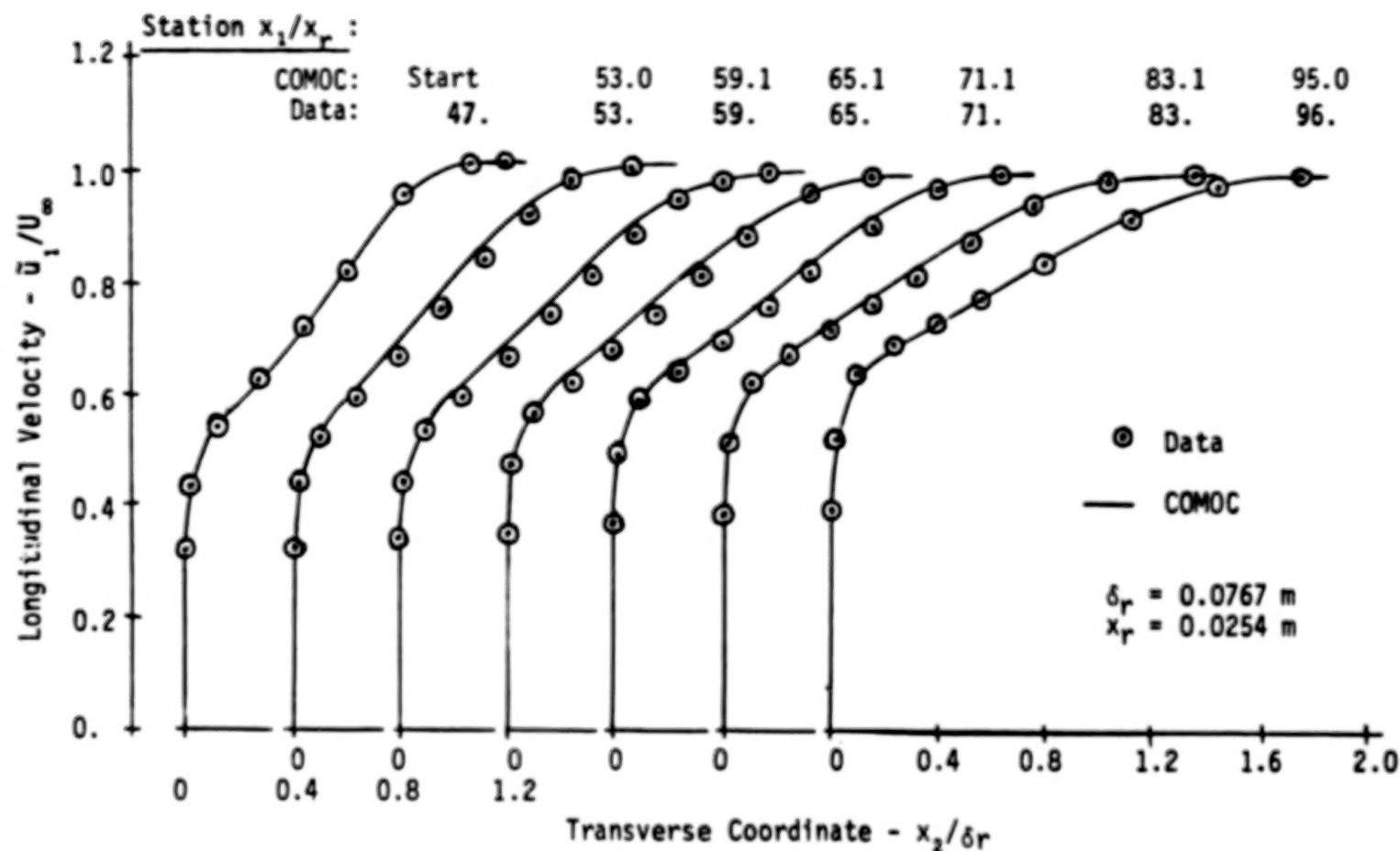


Fig. A.5 Longitudinal Velocity Profiles, Bradshaw Relaxing Flow, MLT

BRADSHAW RELAXING FLOW (IDENT 2400)

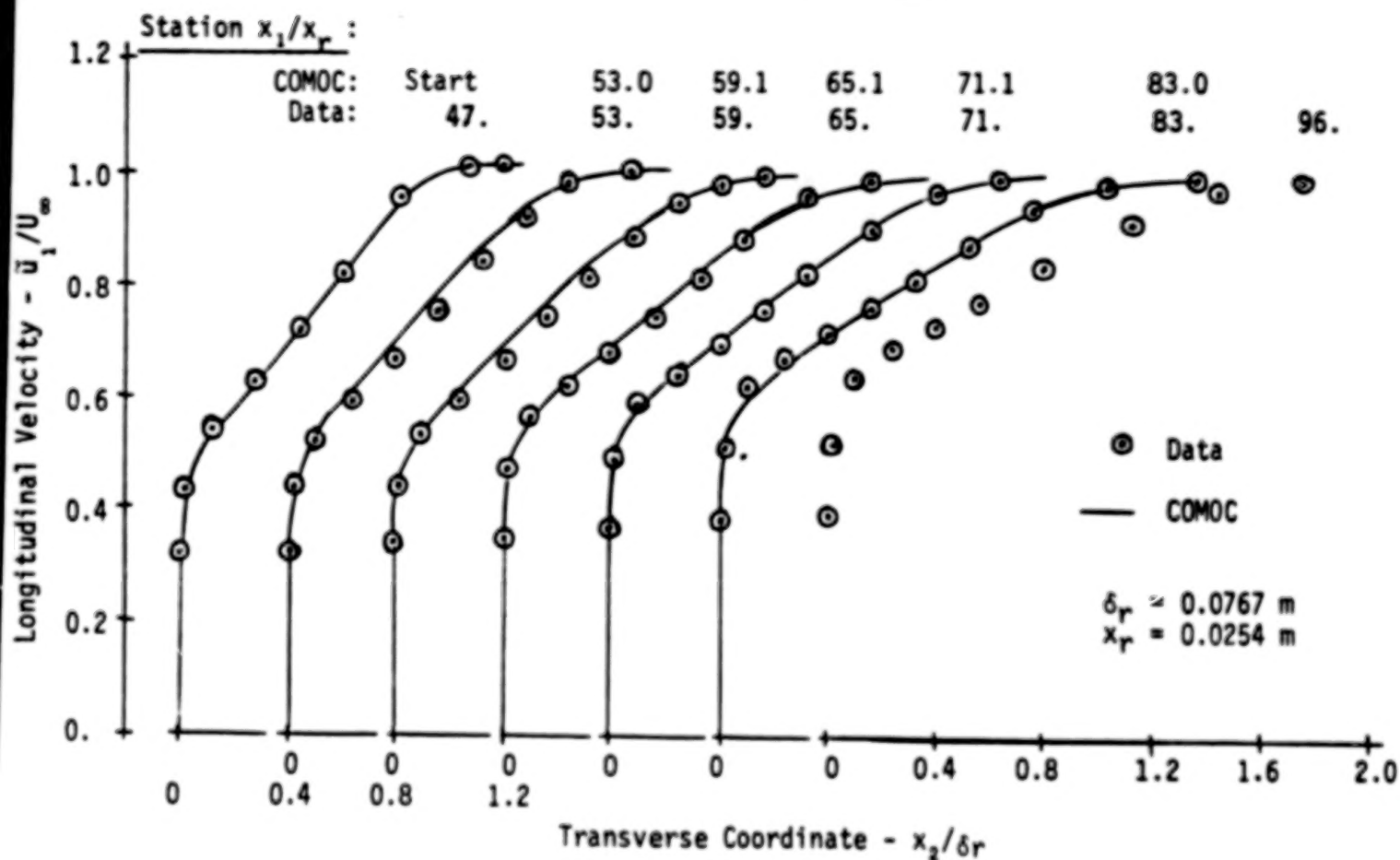


Fig. A.6 Longitudinal Velocity Profiles, Bradshaw Relaxing Flow, TKE

BRADSHAW RELAXING FLOW (IDENT 2400)

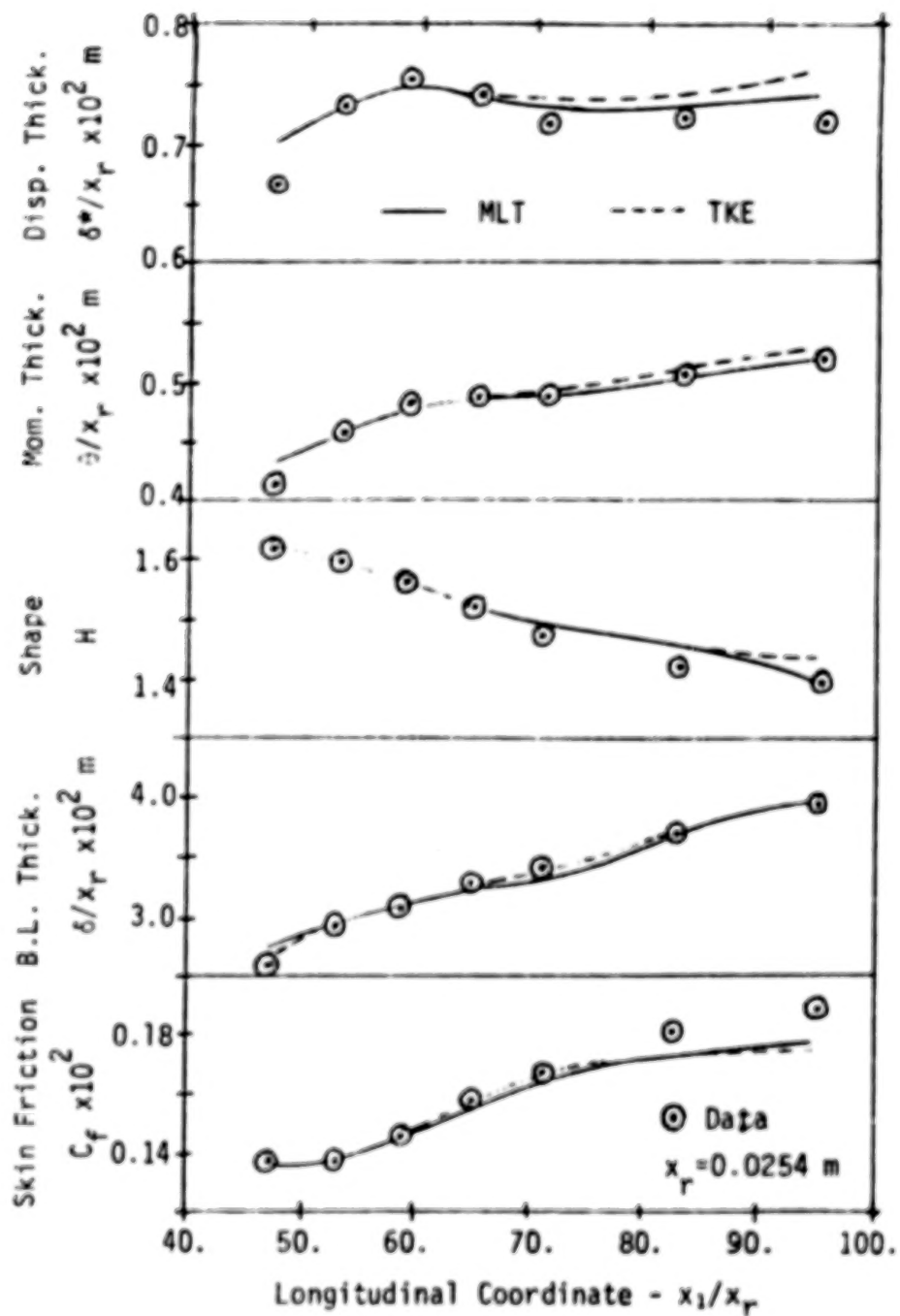


Fig. A.7 Boundary Layer Parameters, Bradshaw Relaxing Flow

REFERENCES

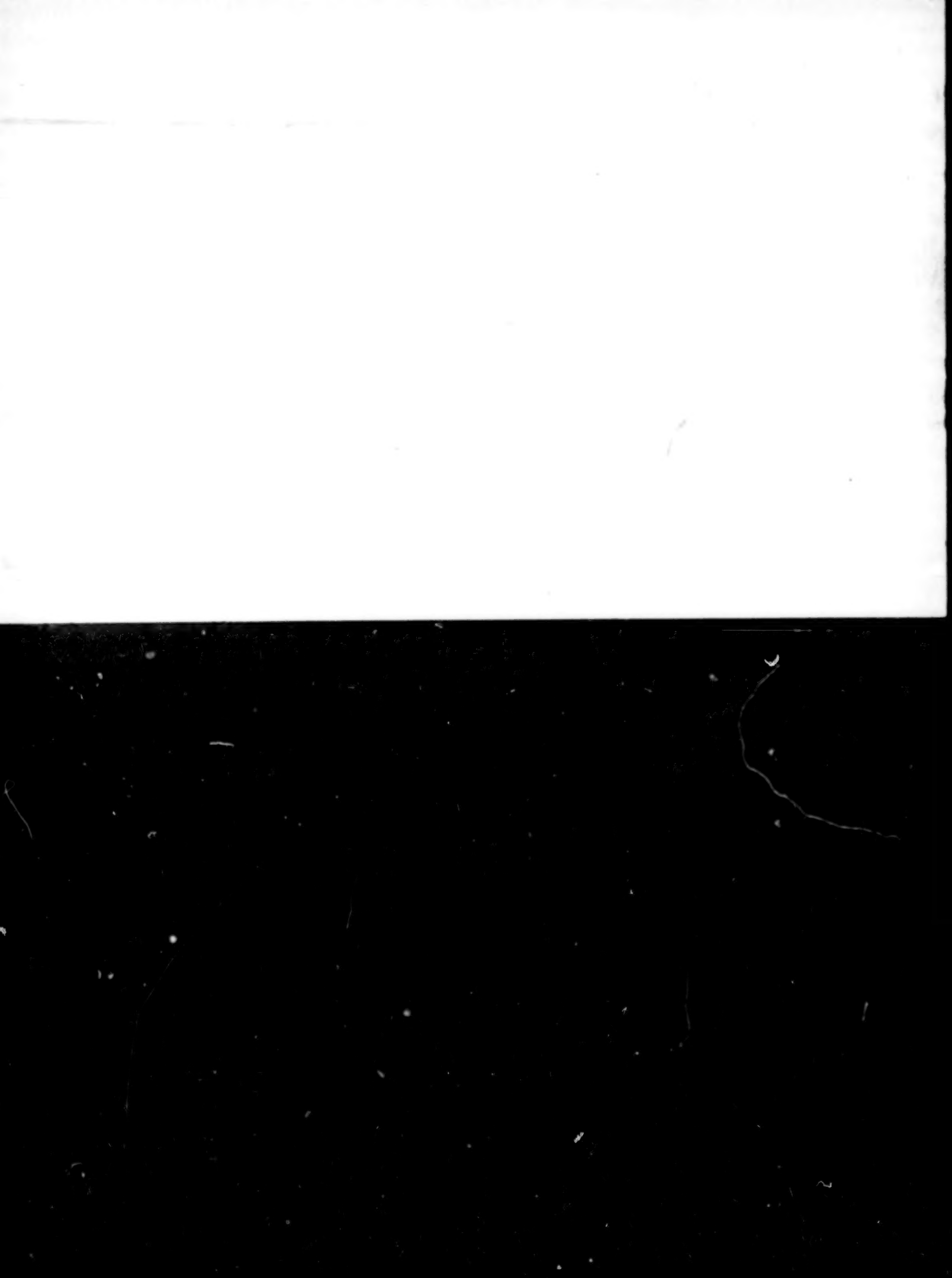
1. Gruschka, H.D. and Schrecker, G.O., "Aeroacoustic Characteristics of Jet Flap Type Exhausts," AIAA Paper 72-130, 1972
2. Lighthill, M.J., "On Sound Generated Aerodynamically, I," Proc. Roy. Soc., A211, pp. 564-587, 1952
3. Lighthill, M.J., "On Sound Generated Aerodynamically, II," Proc. Roy. Soc., A222, pp. 1-32, 1954
4. Reshotko, M., Goodykoontz, H., and Dorsch, R.G., "Engine-Over-The-Wing Noise Research," J. Aircraft, Vol. 11, No. 4, pp. 195-196, 1974
5. Hayden, R.E., Scharton, T.D., Kadman, Y., Wilby, J., and Rudd, M.J., "A Preliminary Evaluation of Noise Reduction Potential for the Upper Surface Blown Flap," NASA CR-112246, 1973
6. Patterson, G.T., Joshi, M.C., and Maus, J.R., "Experimental Investigation of the Aeroacoustic Characteristics of Model Slot Nozzles with Straight Flaps," AIAA Paper No. 75-471, 1975
7. Becker, R.S. and Maus, J.R., "Acoustic Source Location in a Jet-Blown Flap Using a Cross-Correlation Technique," NASA CR-149589, 1977
8. Yee, P.M. "An Experimental and Theoretical Investigation Concerning the Aeroacoustic Characteristics of the Rough Jet Flap," The University of Tennessee, Master's Thesis, 1974
9. Hayden, R.E., Kadman, Y., Chanaud, R.C., "A Study of the Variable Impedance Surface Concept as a Means for Reducing Noise from Jet Interaction with Developed Lift-Augmenting Flaps," NASA CR-112166, 1972
10. Bliss, D.B., and Hayden, R.E., "Exploratory Investigation of Aeroacoustic Optimization of the Variable Impedance Edge Concept Applied to Upper Surface Blown Configurations," NASA CR-2714, 1976.
11. Hersh, A.S., Soderman, P.T. and Hayden, R.E., "Investigation of Acoustic Effects of Leading-Edge Serrations on Airfoils," J. Aircraft, Vol. 11, No. 4, pp. 197-202, 1974
12. Fink, M.R., "Prediction of Airfoil Tone Frequencies," J. Aircraft, Vol. 12, No. 2, pp. 118-120, 1975
13. Bhat, W.V., and Rosso, D.G., "Effect of Forward Speed on Jet Wing/Flap Interaction Noise," AIAA Paper 75-475, 1975

14. O'Brien, V., "Unsteady Cavity Flows: Oscillatory Flat Box Flows," J. App. Mech., pp. 557-563, 1975
15. Wood, D.H. and Antonia, R.A., "Measurements in a Turbulent Boundary Layer Over A d-Type Surface Roughness," J. App. Mech., pp. 591-597, 1975
16. Paterson, R.W. and Amiet, R.K., "Isolated Airfoil - Tip Vortex Interaction Noise," J. Aircraft, Vol. 12, No. 1, pp. 34-40, 1975
17. Reddy, N.N., "Propulsive-Lift Noise of an Upper Surface Blown Flap Configuration," AIAA Paper 75-470, 1975
18. Von Glah, U., and Groesbeck, D., "Nozzle and Wing Geometry Effects on OTW Aerodynamic Characteristics," AIAA Paper No. 76-622, 1976
19. Melnik, R.E. and Chow, R., "Asymptotic Theory of Two-Dimensional Trailing-Edge Flows," NASA SP-347, pp. 177-249, 1975
20. Melnik, R.E. and Chow, R., "Turbulent Interaction at Trailing Edges," NASA CP-2001, pp. 1423-1424, 1976
21. Veldman, A.E.P., "A New Calculation of the Wake of a Flat Plate," J. Engr. Math, V.9, pp. 65-70, 1975
22. Smith, A.M.O. and Cebeci, T., "Remarks on Methods for Predicting Viscous Drag," AGARD-CP-124, 1973
23. Proudman, I., "The Generation of Noise by Isotropic Turbulence," Proc. of Royal Soc., A214, pp. 119-132, 1953
24. Mollo-Christensen, E., and Narasimha, R., "Sound Emission from Jets at High Subsonic Velocities," J. Flu. Mech., Vol. 8, pp. 49-60, 1960
25. Lilley, G.M., "On Noise from Air Jets," ARC, Vol. 20, 1958
26. Moon, L.F. and Zelazny, S.W., "Jet Noise Modeling: Experimental Study and Models for the Noise and Turbulence Fields," AIAA Paper No. 74-3, 1974
27. Csanady, G.T., "The Effect of Mean Velocity Variations on Jet Noise," J. Fluid Mech., Vol. 26, Part 1, pp. 183-197, 1966
28. Patankar, S.V. and Spalding, D.B., Heat and Mass Transfer in Boundary Layers, Second Ed., Intertext, London, 1970

29. Hanjalic', K. and Launder, B.E., "A Reynolds Stress Model of Turbulence and its Application to Thin Shear Flows," J. Flu. Mech. Vol. 52, pp. 609-638, 1972.
30. Tennekes, H. and Lumley, J.L., A First Course in Turbulence, The MIT Press, Cambridge, USA, 1974.
31. Baker, A.J., "A Finite Element Algorithm for the Navier-Stokes Equations," NASA CR -2391, 1974.
32. Cebeci, T. and Smith, A.M.O., Analysis of Turbulent Boundary Layers, Academic Press, New York, 1974.
33. Launder, B.E., Reece, G.J. and Rodi, W., "Progress in the Development of a Reynolds-Stress Turbulence Closure," J. Flu. Mech., Vol. 68, Pt. 3, pp. 537-566, 1975.
34. Launder, B.E. and Spalding, D.B., Lectures in Mathematical Models of Turbulence, Academic Press, London, 1972.
35. Schlichting, H., Boundary-Layer Theory, McGraw-Hill, New York, 1968.
36. Proceedings, AFOSR-IFP-Stanford Conference on Computation of Turbulent Boundary Layers - 1968, Vol. I., Eds. S.J. Kline, G. Sovran, M.V. Morkovan, D.J. Cockrell, Vol. II, Eds. D.A. Coles, E.A. Hirst, pub. by Thermosciences Div., Dept. Mech. Engr., Stanford University 1969.
37. Manhardt, P.D., Orzechowski, J.A., and Baker, A.J., "COMOC II: Two-dimensional Aerodynamics Sequence, Computer Program User's Guide NASA CR-145165, 1977.
38. Schrecker, G.O. and Maus, J.R., "Noise Characteristics of Jet-Flap Type Exhaust Flows," NASA CR - 2342, 1974.
39. Tam, C.K.W. and Reddy, N.M., "Sound Generated in the Vicinity of The Trailing Edge of Upper Surface Blown Flap," AIAA Paper No. 76-503, 1976.
40. Strang, G. and Fix, G.J., An Analysis of the Finite Element Method, Prentice Hall, New Jersey, 1973.

1. Report No. NASA CR-2931		2. Government Accession No.		3. Recipient's Catalog No.	
4. Title and Subtitle Finite Element Analysis of Aeroacoustic Jet-Flap Flows				5. Report Date December 1977	
				6. Performing Organization Code	
7. Author(s) A.J. Baker & P.D. Manhardt				8. Performing Organization Report No. CoMoC 76TR-1.2	
9. Performing Organization Name and Address Computational Mechanics Consultants, Inc. 3601A Chapman Highway Knoxville, TN 37920				10. Work Unit No.	
				11. Contract or Grant No. NAS1-14282	
12. Sponsoring Agency Name and Address National Aeronautics & Space Administration Washington, DC 20546				13. Type of Report and Period Covered Contractor Report	
				14. Sponsoring Agency Code	
15. Supplementary Notes Langley Technical Monitor: Donald L. Lansing Final Report					
16. Abstract <p>A computational analysis is performed on the steady, turbulent aerodynamic flowfields associated with a jet-blown flap. For regions devoid of flow separation, a parabolic approximation to the governing time-averaged Navier-Stokes equations is applied. Numerical results are presented for the symmetry plane flow of a slot-nozzle planar jet flap geometry, including prediction of flowfield evolution within the secondary mixing region immediately downstream of the trailing edge. Using a two equation turbulence kinetic energy closure model, rapid generation and decay of large spatial gradients in mean and correlated fluctuating velocity components within the immediate wake region is predicted. Modifications to the turbulent flow structure, as induced by porous surface treatment of the flap, are evaluated. The recirculating flow within a representative discrete slot in the surface is evaluated, using the two-dimensional, time-averaged Navier-Stokes equations. The parabolic analysis is extended in an introductory manner to a finite span three-dimensional jet-flap flow.</p>					
17. Key Words (Selected by Author(s)) Jet-Flap Flow Turbulent Finite Element Numerical Solution				18. Distribution Statement Unclassified - Unlimited Subject Category 34	
19. Security Classif. (of this report) Unclassified	20. Security Classif. (of this page) Unclassified		21. No. of Pages 68	22. Price* \$5.25	

*For sale by the Clearinghouse for Federal Scientific and Technical Information, Springfield, Virginia 22151.



END

4.19.78